Large Scale Upper-level Precursors for Dust Storm Formation over North Africa and Poleward Transport to the Iberian Peninsula. Part I: An Observational Analysis

J. A. G. Orza[a], S. Dhital[b], S. Fiedler[c], and M. L. Kaplan[d]

[a]SCOLAb, Department of Applied Physics, Universidad Miguel Hernández de Elche, Av. de la Universidad s/n, 03202 Elche, Spain. ja.garcia@umh.es

[b]Division of Atmospheric Sciences, Desert Research Institute, 2215 Raggio Parkway, Reno, NV 89512, USA. sarojdhital11@gmail.com

[c]Institute of Geophysics and Meteorology, University of Cologne, Pohligstrasse 3, 50969 Cologne, Germany. sfiedle6@uni-koeln.de

[d]Applied Meteorology Program, Embry-Riddle Aeronautical University, 3700 Willow Creek Road, Prescott, AZ 86301, USA. kaplanm1@erau.edu

Corresponding author: J. A. G. Orza (ja.garcia@umh.es)

Jose A. Garcia Orza

SCOLAb, Department of Applied Physics

Universidad Miguel Hernandez de Elche

Av. de la Universidad, s/n

03202 Elche (Spain)

Tel. + 34 966658580

Highlights

- Three Saharan dust events with strong impact poleward over the Iberian Peninsula
- A common upper-level precursor for events with substantial subsynoptic differences
- Two polar stream Rossby wave breaks instrumental for dust ablation and transport
- A sequence of multi-scale adjustments organizes the Saharan dust storms

Abstract

The analysis of three extreme African dust outbreaks over the Iberian Peninsula (IP) shows that a double Rossby wave breaking (RWB) process in the polar jet (PJ) creates the conditions for dust storm formation over subtropical deserts in North Africa and the restructuring of upper-level air flows critical for the dust transport poleward after ablation. Two consecutive anticyclonic RWBs initiate over the IP and the adjacent Atlantic, the first commencing 10 days before dust reaches the IP and the second three to five days later. The first RWB becomes quasi-stationary over the eastern Mediterranean when the second RWB develops. In turn, the first RWB blocks downstream propagation of the second, which is amplified by energy reflection poleward from the first break causing vortex intensification and equatorward propagation over the Atlas as well as a strengthening and coupling of the subtropical jet (STJ) to circulations in the ITCZ. Zonal flows are blocked and sustained low-level northeasterlies/easterlies are induced across northwest Africa. The three events present substantial differences in the location and geometry of key upper- and low-level subsynoptic features that organize the dust storms over the Sahara following the second break. Dust lifted by either the cold outflow from convective downdrafts or by orographic gravity waves interacts with terrain-induced and larger scale circulations and is transported to the IP. The location of the cyclonic large scale signal from the second RWB to the west or over the Atlas and the blocking of zonal flows are key for the poleward dust transport.

Keywords: Saharan dust storm, upper-level disturbance, Rossby wave breaking, multi-scale adjustment, poleward dust transport.

1 Introduction

Mineral dust mobilized in dry areas of North Africa impacts the local environment and also distant downwind areas. North African dust emissions are advected primarily to the tropical North Atlantic within the Saharan Air Layer (e.g. Prospero, 1999; Adams et al., 2012; Gläser et al., 2015). Yet, a significant fraction is transported northwards across the Mediterranean (e.g., Moulin et al., 1998; Gkikas et al., 2009; Israelevich et al., 2012; Querol et al., 2009; Pey et al., 2013; Varga et al., 2014; Marinou et al., 2017). Northeasterly/easterly low-level trade winds over northern Africa, commonly referred to as Harmattan winds, prevail in the area and therefore normal conditions do not favor the poleward advection to the Mediterranean and Europe. The intensity of these winds can be modulated by cold air outbreaks in Western Europe resulting in stronger dust transport over the Tropical North Atlantic (e.g., Fiedler et al., 2015; Schepanski et al, 2017). As a consequence, intense dust export has a highly episodic nature.

Much effort has been made in the last decades to characterize the impact over Europe of the African dust outbreaks in terms of aerosol concentrations, composition, and ground-level, column-integrated and vertically-resolved optical properties. That work has resulted in a better knowledge of the spatial extent and variability of that impact, on time scales spanning from diurnal to inter-annual. Similarly, the description of the synoptic scenarios and major pathways leading to dust transport towards Europe has been addressed to a great extent. However, the detailed analysis of the multi-scale atmospheric dynamical processes and features leading to the mobilization of dust in North Africa and its subsequent transport polewards has not received the same attention.

PM_{10} dust concentrations from background air quality monitoring stations and vertically-integrated dust measurements from satellite and sun photometers in the Mediterranean show that both the dust burden and the frequency of dust episodes decrease poleward, as distance increases from the sources (Querol et al., 2009; Pey et al., 2013; Gkikas, 2013). Longitudinal differences are also found, with more dust in spring over the eastern Mediterranean and more dust in summertime over the western part (Moulin, 1998; Gkikas et al., 2009; Israelevich et al., 2012; Querol et al., 2009). Higher PM_{10} concentrations are found in the eastern basin, in part due to the additional contribution of Middle East sources that increase the dust load and also because during summer the dust reaches the western Mediterranean with a great vertical extent and therefore surface concentrations are comparatively lower than the columnar ones (Gkikas et al., 2013; Pey et al., 2013). Dust is the largest contributor to PM_{10} in the regional background sites of Spain (up to 45%), Greece and Cyprus (35%), according to Pey et al. (2013).

The synoptic patterns of poleward transport of dust to the Mediterranean are different in the western and eastern basins (see Varga et al., 2014, for a comprehensive picture of the mean synoptic situations). In the western Mediterranean dust events are dominant in summer and sporadic in spring. Dust is typically transported by southwesterly flows associated with: 1) the intensification and northward migration of the North African High, located above 850 hPa, which transports uplifted dust in its western flank and/or 2) a trough of low pressure extending southwards to northwestern Africa (Rodríguez et al., 2001; Escudero et al., 2005; Salvador et al, 2014; see also Cuevas et al., 2017). In the eastern Mediterranean, dust transport is basically linked to cyclonic activity (Ganor et al., 2010; Dayan et al., 2008; Flaounas et al., 2015), in the form of mid-latitude Mediterranean cyclones and depressions formed in the lee of the Atlas (commonly termed Sharav cyclones). These depressions are displaced east or northeastward along the Mediterranean mostly in spring and winter, carrying dust in the warm sector ahead the cyclone. In the central Mediterranean, summer dust episodes are similar to those of the western part with the governing centers of action located further to the east; in spring, the North African High located over Libya may block the eastward migration of the cyclones and then dust impact is restricted to the central Mediterranean (see Moulin et al., 1998; Israelevich et al., 2002; Barkan et al., 2005).

Moreover, a considerable effort has been made in recent years to identify the dust source areas and the main processes leading to dust entrainment in North Africa (e.g., Knippertz & Todd, 2012, and references therein; Schepanski et al., 2007, 2009; Fiedler et al., 2014, 2015; Pokharel et al., 2017; see also Huneeus et al., 2016). Over the drylands of North Africa, dust is mainly mobilized in deflatable areas by low-level jets, synoptic scale circulations, convective features and downslope winds. In particular the penetration of upper-level troughs into low latitudes represents a large scale forcing on the low-level dynamics associated with intense dust emission episodes over North Africa (e.g., Alpert & Ziv, 1989; Reiff et al., 1986; Barkan et al., 2005; Emmel et al., 2010; Fiedler et al., 2014). Trough amplification and thinning accompanying the equatorward breaking of Rossy waves (RWB) has been observed to trigger heavy precipitation events as well as massive dust mobilization over North Africa (e.g., Thorncroft & Flocas, 1997; Knippertz & Fink, 2006; Fiedler et al., 2015; Wiegand & Knippertz, 2014; Dhital et al., 2020) and the Middle East (e.g., de Vries et al., 2017). The advection of PV-rich and cold air promotes dynamical ascent and a reduction of the static stability that destabilizes the atmosphere. In low-level baroclinic areas it can initiate cyclogenesis (e.g., Thorncroft & Hoskins, 1990; Thorncroft & Flocas, 1997). RWB climatologies show the summer predominance for RWB although breaking waves penetrate far into the subtropics mainly in winter and spring. It is consistently shown that the downstream end of the North Atlantic storm track is a preferred region of RWB (Thorncroft et al., 1993; Postel & Hitchman, 1999; Abatzoglou & Magnusdottir, 2006; Wernli & Sprenger, 2007; Wiegand & Knippertz, 2014).

Although extratropical upper-level disturbances displaced equatorward are found in most major African dust outbreaks in Europe, only a few studies have analyzed in detail the dynamical processes involved in the deflation and the subsequent poleward transport of dust, e.g., Thorncroft & Flocas (1997). Quite recently, Francis et al., (2018) have described an episode of African dust transported to Greenland in which both dust ablation and transport polewards are forced by the Polar Jet.

Three case studies are analyzed in this paper. It is shown that a double Rossby wave break process is the common upper-level large-scale precursor that organizes a favorable environment for dust ablation and poleward transport. The three episodes were driven by anticyclonic Rossby wave breaking (RWB) in the polar troposphere with strong baroclinic forcing of moist convection, which was critical for dust ablation. The cyclonic large scale signal, resulting from positive-tilting and baroclinic trough thinning associated with the double RWB process, triggered convection and was also responsible for dust transport to the Iberian Peninsula (IP). The episodes represent a substantial perturbation of the mean synoptic situation and the strength of both the large scale extratropical cold air intrusion and the organized convection at finer scales is not unrelated to the transitional periods (late summer/early autumn and late winter/early spring) in which they occurred. The cases are also unusual in terms of their impact over the IP. The low-level processes, moisture sources and circulations were distinct in each episode, though they had common large scale precursors at upper-levels.

This paper, Part I, describes the synoptic and larger subsynoptic-scale processes leading to the development of a favorable environment for moist convection or mountain wave formation, dust ablation, and transport to the Iberian Peninsula, while in Part II dust mobilization and transport is described in detail at the finer mesoscales of motion with a high-resolution numerical model and a large number of surface observations.

2 Data and Methods

Data from the European Centre for Medium-Range Weather Forecasts (ECMWF) Interim reanalysis (ERA-Interim; Dee et al., 2011) is used to study the three cases. Data is available at 00, 06, 12 and 18 UTC with 0.75 deg horizontal resolution. Potential vorticity (PV), wind speed and the Montgomery stream function (TSI) on the 330 K isentropic surface are used to analyze the upper-level dynamics and identify RWBs. Higher isentropes are usually preferable for identifying dynamical processes around the subtropical tropopause but the 330 K surface better captures RWBs in the polar stream particularly in such cold events over the North Atlantic and northwestern Europe. Sea level pressure, 2 m air temperature as well as wind speed, potential temperature, and geopotential height at 925 hPa allow the analysis of the near-surface environment. Low-level humidity and convective available potential energy (CAPE) is calculated to support convection initiation. Vertical cross-sections of PV, potential temperature, u-w and v-w wind components, and radiosonde upper-air observations are also analyzed for the interpretation of the case studies.

False-color RGB Dust imagery from the Spinning Enhanced Visual and Infrared Imager (SEVIRI) onboard the geostationary Meteosat Second Generation satellites (MSG), available for both daytime and nighttime with 15 min temporal resolution and a resolution of 3 km at the subsatellite point, is applied to follow the formation and evolution of the dust plumes when not covered by clouds. This imagery also provides information on convective cloud development and low-level moisture that can be associated with moist convection and cold pools as well as haboob formation. RGB dust composites make use of three thermal channels to contrast the brightness temperature signal among surface, cloud, and dust (Lensky and Rosenfeld, 2008) in a color scheme in which dust appears magenta. A number of limitations of the product, including some dependence on column water vapor, lower tropospheric lapse rate, and the altitude of lifted dust, have been identified (see Brindley et al., 2012 and references therein), though this dataset has already proven to be highly useful in most cases. MSG dust imagery supports the description of the smaller scale processes in this paper.

3 Three case studies

All three episodes, i.e., September 2007 (S07), October 2008 (O08) and February 2016 (F16) have already been studied with a focus on their strong impact over the IP by a number of authors. While the October 2008 episode represents a case of extreme impact at the ground level, the September 2007 case is an example of dense dust layers reaching the southern IP at mid-levels in the troposphere, and on February 2016 both middle levels and then the ground were strongly impacted across the IP. MSG dust imagery (Figures 1-3) shows the dust plumes emanating from different source areas over North Africa in each case study and their propagation poleward to the IP.

Very high records of aerosol optical depth (AOD) accompanied by very low Ångström exponent (AE) values were registered on September 6 at Granada during the September 2007 case (Guerrero-Rascado et al., 2009), consistent with the MSG dust imagery in Figure 1h. Only one other episode (on February 2017) has shown substantially higher AODs in southern Spain than this case study. PM_{10} levels were, however, moderate in agreement with the lidar profiles for this event, which identified a thick dust layer at 3-4 km asl over Granada (Guerrero-Rascado et al., 2009). The AOD was also high with low AE at other AERONET stations in southwestern Spain and Portugal during the event (Antón et al., 2012). Figures 1c-1f shows a haboob emanating from a line of convective cells to the southwest of Adrar des Iforas by September 4 that spreads to the northeast and eventually merges with a second haboob generated when convection is triggered in the western slope of the Hoggar. The merger propagates to the northwest and reaches the IP in the early morning of September 9, Figures 1g-1h.

The October 2008 case was the strongest one in terms of PM_{10} concentrations ever registered in a regional background station in southern Spain (Cabello et al., 2012). During the event, up to 89% of the air quality monitoring stations in the country surpassed the 50 $\mu g\ m^{-3}$ EU daily limit value for PM_{10}, with the highest daily mean PM_{10} concentration of 378 $\mu g\ m^{-3}$ found at Malaga on October 11. Zonal winds after October 13 swept the dust plume to western and central Europe, as registered in subsequent days over several countries (see references in Cabello et al., 2012). A haboob starts to become visible on the MSG dust imagery at 13 UTC on September 9, propagating southwestwards from below the convective clouds formed to the south of the Moroccan Atlas (Figure 2d shows the image one hour later). From the early morning of October 10 the dust plume turns cyclonically polewards and reaches southern Spain in the morning of October 11, Figures 2f-2h.

During the February 2016 case, two distinct dust plumes reached the IP one after the other. Both the Iberian Ceilometer Network (Cazorla et al., 2017) and the lidars operating in southeastern and northeastern Spain (Titos et al., 2017) showed elevated plumes at heights below 4000 m at the time of the dust arrival, which subsequently settled down and entrained into the boundary layer. During this episode, 90% of the air quality stations in Spain exceeded the EU daily limit value (Titos et al., 2017). Radiative forcing at the top of the atmosphere in this event was not significantly larger than in other dust episodes (Sorribas et al., 2017) but the intensity was unseasonably strong. The first dust plume starts to be noticeable, Figure 3b, in the foothills of the Saharan Atlas in the MSG dust imagery by 10 UTC, February 20. The plume is elevated and then propagates northwestwards, reaching the IP at 18 UTC (Figure 3e), and is deformed cyclonically over it in the following hours. The second dust plume (Figure 3h) impacted subsequently the eastern IP. It is associated with the outflow from deep convection within the moist tropical plume extending northeastward over North Africa towards the western Mediterranean.

[Figure 1 – Full page]

[Figure 2 – Full page]

[Figure 3 – Full page]

4 Synoptic Scale Environment for Haboob Genesis

4.1 Synoptic Precursor Circulations: Double RWBs

It is important to understand the synoptic precursors that first develop almost ten days prior to the arrival of dust in the Iberian Peninsula. They trigger low-level jet formation processes that lead to dust ablation for all three case studies during which multiple low-level jets develop, most notably but not exclusively: 1) one from the east extending along the Mediterranean coasts of Algeria, Tunisia, and Libya and 2) one from southwestern Algeria that rises up over the Atlas.

The specific synoptic precursors to low-level jets, haboobs, and dust transport in all three cases are remarkably similar in structure and location and all three involve a double RWB in the polar jet stream (PJ) offshore of and over most of Europe. The locations of the RWB do vary longitudinally among the three case studies but what makes them similar and favorable for dust transport poleward to southwestern Europe is how far west in Europe and North Africa they affect. As noted by Postel and Hitchman (1999) and Abatzoglou and Magnusdottir (2006), RWB is accompanied and determined by the unique restructuring of the tropopause, typically depicted on the 350K isentropic surface, in which wave amplification and rotation creates a meridional isentropic potential vorticity (IPV) reversal as well as substantial zonal gradients in IPV. Zonal momentum is converted into eddy momentum by baroclinic and/or barotropic processes. The meridional reversal zone or “surf zone” is often depicted on the 350K isentropic surface and also, more often than not, associated with the subtropical jet stream (STJ). In these three dust storm case studies the evidence points to RWB occurring on the polar tropopause as very cold air is involved in the breaking process consistent with the lower tropopause in the proximity of the polar jet. Because this air involved in the RWBs is so cold in the three case studies, we will focus on IPV on the 330K surface that roughly couples the region in between both upper-level jets in spite of its lack of widespread use in the literature.

Two wave breaks occur, the first commencing roughly ten days prior to dust storm formation in a rather similar manner in all three case studies. Figures 4-6 depict, for all three cases, 330K IPV, wind vectors, and Montgomery stream function (TSI) for the 24-hourly periods for all ten-day 1200 UTC (0000 UTC for F16) analyses including the period five-ten days prior to the arrival of dust over the IP. The meridional IPV reversal on the 330K surface allows identifying the RWBs in these figures and labels indicate their location in each case: “1” is used for the first RWB and “2” for the second RWB, while “3” points in the S07 case to a strengthened PV vortex. While RWB can be cyclonic, in all three case studies both breaks are anticyclonic. The anticyclonic sheared waves break in equatorward direction, consistent with trough thinning equatorward and upstream (i.e., the troughs are oriented in a NE-SW direction) accompanying IPV reversal, as observed in Figures 4-6. As noted in section 2, above, all fields in this paper, Part I, are derived from ECMWF reanalyses and remotely-sensed observations. According to the satellite observations (Figures 1-3), the dust arrives in multiple plumes which follow just 1-3 days after the second wave breaking period. As will be shown in a companion paper, Part II, based on numerical simulations, the plumes of dust are ablated by low-level outflow from massive convection and subsequent haboobs in the S07 and O08 cases, whose organization is tied to circulations established by the two wave breaks. In the F16 case, the combined effects of these circulations and the orographic gravity wave activity force upslope low-level flow over the Saharan Atlas, dust deflation and rising motion. Ultimately these two wave breaking events are instrumental in setting up the low-level mass perturbations and jets that, in turn, organize complex subsynoptic features, i.e., haboobs and confluence zones responsible for dust ablation and its transport poleward.

As noted in Abatzoglou and Magnusdottir (2006), RWB is facilitated when the PJ and STJ are unambiguously split and not continuously linked. Ample proof can be seen depicting this separation of the PJ and STJ ten days before dust arrives over the Iberian Peninsula in Figures 4-6. In all three cases the PJ and STJ are well-developed but separated by a substantial meridional distance along the North African and European Coasts with S07 being quite interesting because the STJ actually resembles a tropical plume structure. This plume is emanating from a tropical disturbance over the North Atlantic consistent with the late summer time period of this event between 30 and 45N. The separation between the two streams is quite evident at the beginning of each period in Supporting Information Figure S1 which represents a precursor period to the first break. In S07, on 26 August the STJ is located primarily between 30 and 45N latitude while the PJ is very close to 60N. In O08 the STJ is equatorward of 30N and PJ roughly at 55N on October 1. In F16 the STJ is between 15 and 30N while the PJ is closer to 45N on February 10. The subsequent RWBs are initiated in the polar stream with very substantial poleward gradients in the Montgomery stream function values on isentropic surfaces indicating very cold air poleward of the PJ (Figures 4-6).

The RWB #1 event occurs from August 28 to August 30 in S07 over the northeastern Atlantic with a substantial strengthening of the IPV gradient over France and northwestern Spain. In O08 the first break occurs from the October 2-4 period reversing the IPV over southern Spain and upstream over the adjacent Atlantic equatorward to coastal North Africa. This is clearly 15-30 degrees west of the S07 break which affects the interior part of western Europe while the O08 is primarily offshore. The F16 break is more closely aligned with the O08 case study thus strengthening the meridional gradient of IPV southwest of Spain over the Atlantic and also over North-west Africa (February 14-16). Accompanying RWB #1, by about seven-eight days before the dust storms, the IPV reversal over western Europe and the eastern Atlantic is complete and the positively-tilted troughs which have formed and the cold air, indicated by low poleward TSI values, transported equatorward into the northern Mediterranean with S07, southern Mediterranean with O08, and northern Africa with F16 in Figures 4-6, respectively. This transport has caused the wind to adjust to the mass resulting in an equatorward and downstream intensification of the STJ in all cases. The STJ was initially maintained as the momentum maxima surrounding the Hadley cell which was well-fortified by very hot air poleward of the Sahara over North Africa or in the case of S07 by an offshore tropical disturbance.

[Figure 4 – Full page]

[Figure 5 – Full page]

[Figure 6 – Full page]

To diagnose the low-level effects of these RWBs, which can be seen in Figures 7-9 at the same time intervals as for Figures 4-6, are depicted the mean sea level pressure, 925 hPa potential temperature, and 925 hPa wind vectors. In these figures the first breaking process has created a low-level signal of positively-tilted troughing over the eastern Mediterranean and ridging poleward over northwestern Europe reflecting the orientation of upper-level troughs and ridges in the wind and TSI fields in Figures 4-6 accompanying the anticyclonic RWB (e.g., Figures 7c, 8c, 9c). Following this initial break, these low-level features will be in place as the second break develops. The features in place with the first break allow favorable conditions for northeasterly-easterly flow along the northern Mediterranean coast of Africa particularly Libya, Tunisia, and Morocco. Specifically, the low-level mass and momentum fields resulting from the first break drift slowly eastward over the Mediterranean into the Middle East and eventually become quasi-stationary in the absence of progressive upstream wave propagation consistent with another major RWB. There, they remain anchored in place and serve to support an upstream-directed low-level pressure gradient and flow directed towards the North African Mediterranean and Atlantic Coastal regions. This serves to block downstream propagation of pressure systems as a lateral boundary condition for the second breaking process (RWB #2) thus facilitating a turning of the upstream flow towards Iberia over northwest Africa. This focuses the development of moist convection and upper-level trough thinning over the northwestern part of Africa allowing transport of dust polewards rather than eastwards.

The literature on RWB, most notably Abatzoglou and Magnusdottir (2006) as well as Strong and Magnusdottir (2008) not only specifies the importance of jet separation in RWB but of such separation in the wave resonance process where energy in the first break is reflected poleward and amplifies the second break. Separation in the jets facilitates poleward energy reflection as opposed to progressive downstream propagation of Rossby waves. This is typically responsible for a massive positive tilt and arching extension of the mass and momentum poleward and downstream with the second break. We see this process occur two-three days after the first break sequence, ~three-five days out in Figures 4-6. As the positively-tilted trough propagates downstream over central and eastern Europe as well as the Mediterranean, a new break begins to form upstream from the anticyclonic IPV on 330K left over from the first break. Consistent with the literature, this second break contains a geometry in the wind and mass fields indicative of even greater positive (anticyclonic) tilt and equatorward as well as poleward penetration of IPV and its meridional reversal as can be seen in Figures 4-6. The equatorward penetration of positive IPV and poleward penetration of negative IPV is even more pronounced than the first break with its motion towards northwestern Africa, i.e., the western Algerian and Moroccan Coasts. This second break is every bit as baroclinic as the first if not more so, with the advection of very low TSI values south-southwestwards and the establishment of a broad scale environment for potential instability over northwest Africa including the region on the leeside of both the Atlas and Hoggar Mountain Ranges in Algeria. In two of the three case studies, i.e., O08 and F16, cutoff vortices result over northwestern Africa in proximity to the Atlas Mountains as a result of this RWB. In S07 an offshore preexisting upstream vortex (labeled as "3" in Figure 4) is fortified by the break downstream over the eastern Mediterranean as energy builds upstream over the eastern Atlantic and that preexisting vortex eventually propagates towards northwest Africa. Figures 4-6 show the sequence of 330K IPV, winds, and TSI for both breaking processes and their general similarity for all case studies. Hovmöller diagrams of PV averaged from 20N to 50N (Figure S2) highlight in a condensed way the progression of the prominent PV features during their migration eastwards, showing a signal of upstream wave reflection organizing the second wave break and changes in the drift rate of the first one induced by the second break.

[Figure 7 – Full page]

[Figure 8 – Full page]

[Figure 9 – Full page]

However, substantial differences are evident among the three case studies in the location and geometry of key upper- and low-level features following the second break and one-three days prior to haboob and dust storm formation in Figures 4-9. In the S07 case, the wave breaking is the farthest poleward and downstream over the northeastern Mediterranean yet it influences the northwestern coast of Africa including the Hoggar and Atlas Mountains. In this case the second break amplifies an offshore vortex west of Portugal that eventually catches up to and becomes entrained into the STJ over northwest Africa. In the O08 case an extremely strong mid-upper tropospheric cutoff vortex forms near the Strait of Gibraltar and continues to amplify equatorward and westwards over the Atlas Mountains. In the F16 case, a similar set of adjustments occurs; however, the mid-upper tropospheric vortex initially forms poleward of Portugal and propagates directly equatorwards down the Atlantic Coast further strengthening over the Atlas. In all three cases, however, these quasi-geostrophic RWBs set up semi-geostrophic jet streak secondary circulations as the periods of wind gust front formation and subsequent dust ablation occur. These circulations in conjunction with terrain-modified circulations organize the potential instability and lift for the haboob-generating dust storm events.

In spite of the differences in the three cases, including the offshore vortex in S07 and the varied subsynoptic jet streak adjustments in all three, there is remarkable similarity in the double RWB mechanisms. The most important similarities include: 1) the first break has a significant downstream dispersive component, 2) the second break is more critical as it is meridionally amplified in the trough thinning process and 3) cold air aloft acts as a unifying signal, not only for the breaking process but for mesoscale adjustments within the jet streaks. Conceptual depictions of the upper- and lower-level features in place are shown in Figures 15 and 16 in the Summary and conclusions section.

Although not the focus of this work, we note that the double Rossby Wave Break process in the Polar Jet implies the large scale forcing of strong cold advection over North Africa that modulates (among others) the intensity and location of the North African High. Cuevas et al (2017) have shown statistically that the North African Dipole Intensity (NAFDI) index and derived metrics change at the intra-seasonal scale driven by the Rossby waves.

4.2 Jet Secondary Circulations, Moist Convective Environments, and Mountain Waves

The RWBs act as space-time boundary conditions and establish complex jet streak adjustments at semi-geostrophic motions scales, i.e., contracting 2500-5000 km Rossby wave forcing down to ~1000 km or smaller scale secondary circulations in the PJ and STJ. As the second break occurs, jets intensify and produce circulations with stronger accelerating flow than the larger RWBs can produce. Cold fronts strengthen and make anomalous penetrations deep into Africa. The first RWB blocks the rapid downstream propagation of the STJ and PJ. Also, the STJ is strengthened by the first RWB as its cold air is advected into North Africa from northwestern Europe. Furthermore, the massive vortices formed aloft (O08 and F16) or enhanced

(S07) by the second baroclinic RWB contain newly formed southerly momentum and these new PJ streaks are in place and available to interact with the streaks in the STJ enhanced by the equatorward advection of cold air. The hot air over the Algerian and neighboring Saharan deserts are also fortifying the streaks aloft by intensifying the TSI gradients on theta surfaces on the anticyclonic side of the jets. Hence, prior to a day or two of the developing dust storms, the entrance region of the STJ is propagating poleward and downstream over eastern Algeria and neighboring countries and the exit region of the PJ is approaching the STJ entrance region over primarily Algeria and are both now positioned such that the semi-geostrophic secondary circulations can mutually interact. This interaction favors deep ascent as the PJ and STJ lift air at different vertical levels which realizes the potential instability and results in moist convection in the S07 and the O08 cases; in the F16 case, the jet streaks-induced deep ascent aids in the destabilization process where surface heating is occurring as the air is adiabatically cooling above the surface sensible heating in the southern slope of the Saharan Atlas. Since this occurs over northwest Africa in proximity to the Saharan heat low, the mass perturbations caused by this heat low and differential heating along the slopes of the mountains also strengthens the jet circulations aloft. This interaction location between the STJ and PJ is also in proximity to hot air over the Algerian deserts east of the Atlas, cool offshore maritime Atlantic air west of Morocco, and relatively warm and moist air over the Mediterranean forced westwards by the mass and momentum fields remaining from the first break. In addition, in S07, very warm and moist air from the Intertropical Convergence Zone (ITCZ) equatorwards of Algeria over Mali whose motion westwards and poleward is enhanced by the Tropical Easterly Jet (TEJ) as well as the anticyclonic gyre as the STJ strengthens and rotates across northeastern Africa in O08 and F16. These multi-scale processes produce differing air masses and vertically differential air mass advection which are in proximity to produce moist convection in this region between the Atlas and Hoggar Mountains and the Mediterranean.

[Figure 10 – Full page]

Figure 10 depicts vertical cross sections of winds, potential temperatures, and vertical motions just prior to the images of developing convection and mountain wave activity. Figures 11 and 12 show distributions of convective available potential energy (CAPE) and low-level relative humidity (RH) for the S07 and O08 cases. Subsequent cold convective cloud tops are followed by dust ablation in MSG imagery depicted in Figures 1c-1f and 2c-2e for the S07 and O08 case studies. The timing of these figures in the two cases is to show massive Mesoscale Convective System (MCS) formation organizing haboobs on the windward side of the Hoggar for S07 (see CAPE in Figures 11h, 11i) and leeside of the Atlas for O08 (see Figure 12h). Where windward and leeside refer to the mid-upper tropospheric predominantly westerly flow in each case study. Figure 13 shows the near-surface air temperature and wind vector for the F16 case study at noontime. Southerly warm dry air on the foothills of the Atlas precedes the terrain-induced heating perturbations (Figure 13g) accompanying dust ablation shown in MSG imagery in Figures 3b-3d. The organizing mechanisms for the environment triggering convection involves the development of ascent in jet secondary circulations resulting from the two RWBs described above as well as extreme differential heating between the Hoggar and Atlas Mountain slopes and the nearby atmosphere consistent with a mountain-plains solenoidal circulation (MPS) (e.g., Tripoli & Cotton, 1989; Zhang & Koch, 2000). The MPS enhances the jet circulations both: 1) directly by accompanying lifting in the warm air along the mountainside exposed to solar radiation as well as planetary boundary layer (PBL) deepening and 2) indirectly by enhancing the accelerations and upper-level divergence due to increasing TSI gradients on that surfaces in both the newly-intensifying balanced semi-geostrophic and thermally direct STJ entrance region secondary circulation and newly-intensifying PJ exit region circulations for each case study.

[Figure 11 – Full page]

[Figure 12 – Full page]

[Figure 13 – Full page]

These circulations are depicted for the three case studies along meridional vertical cross sections in Figure 10 located so as to parallel the MCS genesis processes over the mountains flanking 0 degrees longitude. These vertical cross sections should be compared to Figures 7-9 and 11-13 which indicate general inverted low-level troughs oriented west-northwest – east-southeast in all cases with even stronger low-level troughs oriented northeast-southwest in O08 and F16. These troughs are flanked by cutoff mid-upper tropospheric lows over the Atlas for these two cases and an offshore low for S07. A broader scale Saharan heat low exists over western and central Algeria. The areas of key ascent in the vertical cross sections in Figure 10 and corresponding jet secondary circulations in the horizontal cross sections (at the 330 K surface) in Figures 4-6 are marked with a green circle. In S07 as depicted in Figure 10a, ascent near 25N and 2.5E at 1200 UTC September 4 is ahead of the polar front located just equatorward of 30N and strongly coupled to the anticyclonic and diverging flow in the right entrance region of the STJ between 600 and 300 hPa. This is above the haboobs triggered on the western slopes of the Hoggar Mountains. In O08, the key upper-level circulation is the left jet exit region ascent between 30 and 35N along 2.5W at 1200 UTC on October 8 in Figure 10b. This indirect circulation flanks a remarkably deep cold front aloft between 700 and 200 hPa and acts to strengthen it in time. This ascent slices through the 330 K surface. This circulation supports the lifting and destabilization over northwest Algeria on the northeastern slopes of the Atlas Mountains. Haboob genesis here is strongly controlled by the deep cold air advection and left exit region ascent accompanying the diverging flow. In F16 between 1200 UTC February 19 and 0000 UTC February 20 as depicted in Figure 10c, the ascent from the polar and subtropical jets' left exit regions controls the regeneration of convection along the cold front over the northern slopes of the Hoggar Mountains. Here the ascent shifts somewhat equatorward of the dual jets' left exit regions indicating a possible unbalanced component to the upper-level diverging flow extending southeastwards across the Hoggar Mountain range.

The low-level jets at 925 hPa in Figures 7-9 reflect the confluence of Mediterranean moisture from the east, extreme Algerian heat fortified along the Hoggar and Atlas Mountain slopes from the south-southwest, and cooler onshore flow from the Atlantic to the west-northwest. The patterns of CAPE and RH reflect the moist air from the Mediterranean and moist monsoonal air from the ITCZ undercutting hot dry Saharan air. These maxima of CAPE in the preconvective environment are formed as the cold mid-upper tropospheric vortices propagate equatorward and, in conjunction with ascent in the jet secondary circulations described in the previous paragraph, they advect cold air equatorward and lift the air, respectively. The higher CAPE air masses then organize massive moist convective systems. The favorable environment for moist convection, for example, is dramatically depicted in Figure 14 where the 24-hour changes in the Dar-El-Beida (DAAG) soundings are inter compared during haboob genesis on the slopes of the Atlas (Figure 2). Note in Figure 14 the shift in flow to the east under hot dry adiabatic conditions aloft and substantial increase in sounding CAPE between the early and late time periods. This is typical of a well-mixed layer aloft being undercut by moist Mediterranean air as cold air arrives in the jet exit region. This sounding is located under the equatorward amplifying upper-level IPV maximum and the right entrance region of the STJ over North Africa during O08 in Figures 4 and 10b as well. Mid-upper tropospheric cooling occurs in conjunction with the advection of moist air under the well-mixed layer. In S07 the right entrance region of the STJ is fortified by the outflow above tropical convection from the right exit region of the TEJ in Figure 10a. In F16 a somewhat similar coupling of strong STJ exit region ageostrophic flow and inflow from the ITCZ is evident in Figures 6 and 10c. Thus in all three cases the favorable environment for deep MCS and MPS formation on the slopes of the mountains results from the mid-latitude multiple RWBs as the PJ and STJ exit and entrance regions are restructured by those wave breaking processes. As a result, moist convection develops from southwest to northeast in S07 along the slopes of the Hoggar, orographic gravity wave activity builds up first over the northern slopes of the Hoggar and then in the southern slopes of the Saharan Atlas in F16 and very persistent multiple MCS form in O08 primarily on the downstream leeside of the northern Atlas.

Figures 1-3 indicate that plumes of dust emanate from the convection or from the terrain-induced wave activity as these features develop. In S07, convection builds northeastwards up the windward slope of the Hoggar. Two distinct MCS form first near the Algerian border with Mali and second northeast over western Algeria with each indicating a haboob. The haboobs generate low-level outflow and the subsequent spreading of dust, first from the southwest with the first MCS and then towards the northwest with the second MCS in Figure 1. These plumes merge and turn northwestwards in the confluence zone between northeasterly low-level flow over northeastern Algeria and southwesterly low-level flow over central Algeria in Figure 7. Aloft, the lift for this convection is anchored in the region where the TEJ right exit region (Figure 4) is fortified by moist convection and parcels are then turning into and accelerating into the STJ right entrance region creating both speed and curvature-induced divergence in the upper troposphere above a well-heated and well-mixed convective PBL over the Hoggar in Figure 10a. The arrival of the mid-upper tropospheric offshore vortex in the STJ further lifts parcels rich in dust as the low-level plume resulting from the merger of the two haboobs (Figure 1) approaches the Atlas Mountains in the right exit region of the jet streak preceding the vortex.

In O08, persistent convection along the northwest African Coast extending downstream across the northern Atlas Mountains organizes a haboob that propagates southwestwards towards an inland propagating Atlantic onshore cool front in Figure 2. The motion of the strong dust front is controlled by the Atlas guiding it southwestwards as it converges into an onshore flow of cool Atlantic air equatorward of the Atlas as can be seen in the low-level flow in Figure 8. This dust plume eventually turns northwards and then northwestwards (Figure 2) and is converged into a cyclonic circulation in proximity to the downstream hot air in the Saharan heat low over southcentral Algeria. It is subsequently joined by another plume of dust from a smaller MCS that formed close to the Hoggar. These plumes converge, take on a cyclonic coma shape, and turn north-northwestwards in the confluence zone setup by the merger of southeasterly hot air from the Saharan heat low, northeasterly cool air from the haboob and Mediterranean, and westerly cool airflow from the Atlantic. It is shown in Figure 8 that a new subsynoptic surface low forms here as the dust is lifted over the Atlas. The plumes are also lifted by the strong jet entrance region circulation from the STJ but more dramatically by the new PJ streak that formed ahead of the mid-upper tropospheric vortex, which transports the dust over the Atlas towards the Strait of Gibraltar and the Spanish Coast in Figure 10b.

Finally, in F16, a strong downslope wind over the northern slope of the Hoggar Mountains forms under a highly accelerative region in the STJ entrance which is subsequently but closely followed by very intense lifting in the exit region of a PJ streak ahead of the vortex analogous to O08 in Figure 10c. However, the dust transport northwestwards in this case (Figure 3) is facilitated by increasing southeasterly flow up the Atlas after a break period during which the PJ streak propagates over the Atlas and the Strait of Gibraltar. Remarkably strong terrain-induced waves analogous to terrain-induced gravity waves form above the Atlas during this transport process and likely control the lifting of the dust towards Iberia under an accelerating polar jet streak entrance ahead of the upper vortex in Figure 6. These waves may also reflect the strong divergence in the right exit region of this streak indicative of an unbalanced jet circulation during a period of substantial surface heating over the Saharan Atlas Mountains similar to the unbalanced circulations described in Pokharel et al. (2016).

[Figure 14 – Full width]

5 Summary and Conclusions

A sequence of multi-scale adjustments starting from continental scales and cascading down the scale of MCS are implicated in organizing multiple Saharan dust storms prior to dust transport poleward above the Iberian Peninsula. Two polar stream Rossby wave breaks represent the large scale organizing mechanisms with the first commencing nearly ten days prior to dust storm formation followed by a second three to five days later. As the two RWBs occur, both the PJ and STJ are radically restructured as is implicit in the IPV reversal process. This restructuring involves vortex intensification and equatorwards propagation during the trough thinning process over the Atlas Mountains as well as a strengthening and coupling of the STJ to circulations in the ITCZ. New PJ streaks intensify downstream from these vortices. These southwesterly streaks enhance mid-upper tropospheric cyclone formation upstream and over the Atlas and also produce low-level jets that transport hot low-level air poleward that interact with persistent cooler and moist low-level jets from the Mediterranean coastal region. MCS develop as the hot Saharan air overruns the cooler moist Mediterranean air and/or the very moist air from the ITCZ and subsequently is lifted by the jet streak secondary circulations as the cold mid-tropospheric air with each upper vortex is transported towards the equator. The potential instability that forms and is triggered by jet streak lifting generates deep and widespread MCS formation which is critical to haboob genesis that ablates surface dust. Also it is the proximity of PBL outflow from the MCS to sources of dust, deep ascent poleward of the dust generation region, and subsequent poleward transport that is critical to dust arriving over Iberia. That outflow lifts the dust and then the dust interacts with complex terrain-induced and larger scale circulations. Schematics of these complex processes as derived in this first paper from observations are depicted in Figures 15-16.

The double RWB mechanism, linked to nonlinear wave reflection, ultimately favors the poleward transport of dust to the Iberian Peninsula, rather than eastwards, both by the amplification of the second RWB and trough thinning west or over the Atlas and by blocking zonal air flows. Perhaps the most important result of the analyses is the dominance of the polar jet, its extraordinary cold air, and its strong coupling to anticyclonic RWB. In all three case studies there is a remarkable equatorward penetration of polar air into Africa that represents an extreme cold air anomaly at progressively lower latitudes in Africa as the case studies transition from summer to autumn to winter. In fact, the signal of over-reflection is consistent with the findings of Abatzoglou & Magnusdottir (2006), but for RWBs in the polar stream over Europe in transition seasons as opposed to exclusively the subtropical tropopause over the Pacific and the Atlantic in the warm season. These authors have found non-linear reflection in a large proportion of RWBs; therefore, a large climatology of RWBs in the polar stream, including the assessment of non-linear reflection, and its implication in organizing Saharan dust storms is of relevance and will be conducted in the future.

[Figure 15 – Full width]

The analysis in this first paper is derived solely from observations, as such it is lacking in detail possible in space and time from high resolution numerical model simulations. It represents a broad overview of the processes that lead to dust storms and dust transport from the Sahara to the IP in three case studies. Numerical simulations of meso-α, β, and γ-scale air trajectories and PBL circulations in proximity to complex terrain and in comparison to surface and remotely-sensed atmospheric optical depth observations of dust will be analyzed in a subsequent paper, Part II, to follow. This will enable a truly mesoscale analysis of the broader scale observationally-derived features described in this paper.

[Figure 16 – Full width]

Acknowledgments and Data

This work is partially funded by the Spanish Ministerio de Economía y Competitividad and EU FEDER under grant CGL2015-70741-R (FRESA Project). J.A.G.O. acknowledges the Regional Government of Valencia (grant BEST/2018/091) for partial support of a research visit at DRI in summer 2018, and thanks DRI and Prof. Kaplan for hosting him.

We thank ECMWF for making available the ERA-Interim reanalysis data (https://www.ecmwf.int/en/forecasts/datasets/reanalysis-datasets/era-interim), EUMETSAT for the SEVIRI MSG data (available at https://eoportal.eumetsat.int/ after registration), NOAA/ESRL for the provision of the HYSPLIT model, and the University of Wyoming for providing access to their radiosounding database.

References

Abatzoglou, J.T., & Magnusdottir, G. (2006). Planetary wave breaking and nonlinear reflection: Seasonal cycle and interannual variability. Journal of Climate, 19, 6139–6152. https://doi.org/10.1175/JCLI3968.1

Adams, A.M., Prospero, J.M., & Zhang, C. (2012). CALIPSO-derived three-dimensional structure of aerosol over the Atlantic basin and adjacent continents. Journal of Climate, 25, 6862–6879. https://doi.org/10.1175/JCLI-D-11-00672.1

Alpert, P., & Ziv, B. (1989). The Sharav cyclone - observations and some theoretical considerations. Journal of Geophysical Research, 94(D15), 18,495–18,514. https://doi.org/10.1029/JD094iD15p18495

Antón, M., Sorribas, M., Bennouna, Y., Vilaplana, J.M., Cachorro, V.E., Gröbner, J., Alados-Arboledas, L. (2012). Effects of an extreme desert dust event on the spectral ultraviolet irradiance at El Arenosillo (Spain). Journal of Geophysical Research: Atmospheres, 117, D03205. https://doi.org/10.1029/2011JD016645

Barkan, J., Alpert, P., Kutiel, H., & Kishcha, P. (2005). Synoptics of dust transportation days from Africa toward Italy and central Europe. Journal of Geophysical Research: Atmospheres, 110, D07208. https://doi.org/10.1029/2004JD005222

Brindley, H., Knippertz, P., Ryder, C., & Ashpole, I. (2012). A critical evaluation of the ability of the Spinning Enhanced Visible and Infrared Imager (SEVIRI) thermal infrared red-green-blue rendering to identify dust events: Theoretical analysis. Journal of Geophysical Research, 117, D07201. https://doi.org/10.1029/2011JD017326

Cabello, M., Orza, J.A.G., Barrero, M.A., Gordo, E., Berasaluce, A., Cantón, L., et al. (2012). Spatial and temporal variation of the impact of an extreme Saharan dust event. Journal of Geophysical Research, 117, D11204. https://doi.org/10.1029/2012JD017513

Cazorla, A., Casquero-Vera, J.A., Román, R., Guerrero-Rascado, J.L., Toledano, C., Cachorro, V.E., et al. (2017). Near-real-time processing of a ceilometer network assisted with sun-photometer data: monitoring a dust outbreak over the Iberian Peninsula. Atmospheric Chemistry and Physics 17, 11,861–11,876. https://doi.org/10.5194/acp-17-11861-2017

Cuevas, E., Gómez-Peláez, A.J., Rodríguez, S., Terradellas, E., Basart, S., García, O.M. & Alonso-Pérez, S. (2017). The pulsating nature of large-scale Saharan dust transport as a result of the interplays between mid-latitude Rossby waves and the North African Dipole Intensity. Atmospheric Environment 167, 586-602. https://doi.org/10.1016/j.atmosenv.2017.08.059

Dayan, U., Ziv, B., Shoob, T., & Enzel, Y. (2008). Suspended dust over southeastern Mediterranean and its relation to atmospheric circulations. International Journal of Climatololgy, 28, 915–924. https://doi.org/10.1002/joc.1587

Dee, D.P., et al. (2011). The ERA-Interim reanalysis: Configuration and performance of the data assimilation system. Quarterly Journal of the Royal Meteorological Society, 137, 553–597. https://doi.org/10.1002/qj.828

De Vries, A.J., Ouwersloot, H.G., Feldstein, S.B., Riemer, M., El Kenawy, A.M., McCabe, M.F., Lelieveld, J. (2018). Identification of tropical-extratropical interactions and extreme precipitation events in the Middle East based on potential vorticity and moisture transport. Journal of Geophysical Research: Atmospheres, 123, 861–881. https://doi.org/10.1002/2017JD027587

Dhital, S., Kaplan, M.L., Orza, J.A.G., Fiedler S. (2020). Atmospheric Dynamics of a Saharan Dust Outbreak over Mindelo, Cape Verde Islands: Multi-scale Observational Analyses and Simulations. Manuscript submitted for publication.

Emmel, C., Knippertz P., Schulz, O. (2010) Climatology of convective density currents in the southern foothills of the Atlas Mountains. Journal of Geophysical Research, 115, D11115, doi:10.1029/2009JD012863

Escudero M., Castillo S., Querol X., Avila A., Alarcón M., Viana M.M., et al. (2005). Wet and dry African dust episodes over Eastern Spain. Journal of Geophysical Research, 110, D18S08. https://doi.org/10.1029/2004JD004731

Fiedler, S., Schepanski, K., Knippertz, P., Heinold, B., & Tegen, I. (2014). How important are atmospheric depressions and mobile cyclones for emitting mineral dust aerosol in North Africa? Atmospheric Chemistry and Physics, 14(17), 8983–9000. https://doi.org/10.5194/acp-14-8983-2014

Fiedler, S., Kaplan, M.L., & Knippertz, P. (2015). The importance of Harmattan surges for the emission of North African dust aerosol. Geophysical Research Letters, 42, 9495–9504. https://doi.org/10.1002/2015GL065925

Flaounas, E., Kotroni, V., Lagouvardos, K., Kazadzis, S., Gkikas, A., & Hatzianastassiou, N. (2015). Cyclone contribution to dust transport over the Mediterranean region. Atmospheric Science Lettters, 16, 473–478. https://doi.org/10.1002/asl.584

Francis, D., Eayrs, C., Chaboureau, J.-P., Mote, T., & Holland, D.M. (2018). Polar Jet Associated Circulation Triggered a Saharan Cyclone and Derived the Poleward Transport of the African Dust Generated by the Cyclone. Journal of Geophysical Research: Atmospheres, 123, 11,899–11,917. https://doi.org/10.1029/2018JD029095

Ganor, E., Osetinsky, I., Stupp, A., & Alpert, P. (2010). Increasing trend of African dust, over 49 years, in the eastern Mediterranean. Journal of Geophysical Research, 115, D07201. https://doi.org/10.1029/2009JD012500

Gkikas, A., Hatzianastassiou, N., & Mihalopoulos, N. (2009). Aerosol events in the broader Mediterranean basin based on 7-year (2000–2007) MODIS C005 data. Annales Geophysicae, 27, 3509–3522. https://doi.org/10.5194/angeo-27-3509-2009

Gkikas, A., Hatzianastassiou, N., Mihalopoulos, N., Katsoulis, V., Kazadzis, S., Pey, J., et al. (2013). The regime of intense desert dust episodes in the Mediterranean based on contemporary satellite observations and ground measurements. Atmospheric Chemistry and Physics, 13, 12,135–12,154. https://doi.org/10.5194/acp-13-12135-2013

Gläser, G., Wernli, H., Kerkweg, A., & Teubler, F. (2015). The transatlantic dust transport from North Africa to the Americas–Its characteristics and source regions. Journal of Geophysical Research: Atmospheres, 120, 11,231–11,252. https://doi.org/10.1002/2015JD023792

Guerrero-Rascado, J.L., Olmo, F.J., Avilés-Rodríguez, I., Navas-Guzmán, F., Pérez Ramírez, D., Lyamani, H., & Alados Arboledas, L. (2009). Extreme Saharan dust event over the southern Iberian Peninsula in september 2007: active and passive remote sensing from surface and satellite. Atmospheric Chemistry and Physics, 9, 8453–8469. https://doi.org/10.5194/acp-9-8453-2009

Huneeus, N., Basart, S., Fiedler, S., Morcrette, J.-J., Benedetti, A., Mulcahy, J., Terradellas, E., Pérez García-Pando, C., Pejanovic, G., Nickovic, S., Arsenovic, P., Schulz, M., Cuevas, E., Baldasano, J.M., Pey, J., Remy, S., and Cvetkovic, B. (2016). Forecasting the North

African dust outbreak towards Europe in April 2011: a model intercomparison, Atmospheric Chemistry and Physics, 16, 4967-4986. https://doi.org/10.5194/acp-16-4967-2016

Israelevich, P.L., Levin, Z., Joseph, J.H., & Ganor, E. (2002). Desert aerosol transport in the Mediterranean region as inferred from the TOMS aerosol index. Journal of Geophysical Research, 107(D21), 4572. https://doi.org/10.1029/2001JD002011

Israelevich, P., Ganor, E., Alpert, P., Kishcha, P., & Stupp, A. (2012). Predominant transport paths of Saharan dust over the Mediterranean Sea to Europe. Journal of Geophysical Research, 117, D02205. https://doi.org/10.1029/2011JD016482

Knippertz, P. & Fink, A.H. (2006). Synoptic and dynamic aspects of an extreme springtime Saharan dust outbreak. Quarter Journal of the Royal Meteorological Society, 132, 1153–1177. doi: 10.1256/qj.05.109

Knippertz, P., & Todd, M.C. (2012). Mineral dust aerosols over the Sahara: meteorological controls on emission and transport and implications for modeling. Reviews of Geophysics, 50, RG1007. https://doi.org/10.1029/2011RG000362

Lensky, I.M. and Rosenfeld, D. (2008). Clouds-Aerosols-Precipitation Satellite Analysis Tool (CAPSAT). Atmospheric Chemistry and Physics, 8, 6739–6753. https://doi.org/10.5194/acp-8-6739-2008

Marinou, E., Amiridis, V., Binietoglou, I., Tsikerdekis, A., Solomos, S., Proestakis, E., et al. (2017). Three-dimensional evolution of Saharan dust transport towards Europe based on a 9-year EARLINET-optimized CALIPSO dataset. Atmospheric Chemistry and Physics, 17, 5893–5919. https://doi.org/10.5194/acp-17-5893-2017

Moulin, C., Lambert, C.E., Dayan, U., Masson, V., Ramonet, M., Bousquet, P., et al. (1998). Satellite climatology of African dust transport in the Mediterranean atmosphere. Journal of Geophysical Research, 103(D11), 13,137–13,144. https://doi.org/10.1029/98JD00171

Pey, J., Querol, X., Alastuey, A., Forastiere, F., & Stafoggia, M. (2013). African dust outbreaks over the Mediterranean Basin during 2001–2011: PM10 concentrations, phenomenology and trends, and its relation with synoptic and mesoscale meteorology. Atmospheric Chemistry and Physics, 13, 1395–1410. https://doi.org/10.5194/acp-13-1395-2013

Pokharel, A.K., Kaplan, M.L., & Fiedler, S. (2017). Subtropical Dust Storms and Downslope Wind Events. Journal of Geophysical Research: Atmospheres, 122, 10,191–10,205. https://doi.org/10.1002/2017JD026942

Postel, G.A., & Hitchman, M.H. (1999). A climatology of Rossby wave breaking along the subtropical tropopause. Journal of the Atmospheric Sciences, 56, 359–373. https://doi.org/10.1175/1520-0469(1999)056<0359:ACORWB>2.0.CO;2

Prospero, J.M. (1999). Long-term measurements of the transport of African mineral dust to the southeastern United States: Implications for regional air quality. Journal of Geophysical Research, 104, 15,917–15,928. https://doi.org/10.1029/1999JD900072

Querol, X., Pey, J., Pandolfi, M., Alastuey, A., Cusack, M., Pérez, N., et al. (2009). African dust contributions to mean ambient PM10 mass-levels across the Mediterranean Basin.

Atmospheric Environment, 43, 4266–4277. https://doi.org/10.1016/j.atmosenv.2009.06.013

Reiff J., Forbes G.S., Spieksma F.Th.M., Reynders J.J. (1986). African dust reaching Northwestern Europe: A case study to verify trajectory calculations. Journal of Climate and Applied Meteorology, 25 (11),1543–1567.

Rodríguez, S., Querol, X., Alastuey, A., Kallos, G., & Kakaliagou, O. (2001). Saharan dust contributions to PM10 and TSP levels in Southern and Eastern Spain. Atmospheric Environment, 35, 2433–2447. https://doi.org/10.1016/S1352-2310(00)00496-9

Salvador, P., Alonso-Pérez, S., Pey, J., Artíñano, B., de Bustos, J.J., Alastuey, A., & Querol, X. (2014). African dust outbreaks over the western Mediterranean Basin: 11-year characterization of atmospheric circulation patterns and dust source areas. Atmospheric Chemistry and Physics, 14, 6759–6775. https://doi.org/10.5194/acp-14-6759-2014

Schepanski, K., Tegen, I., Laurent, B., Heinold, B., & Macke, A. (2007). A new Saharan dust source activation frequency map derived from MSG-SEVIRI IR channels. Geophysical Research Letters, 34, L18803. https://doi.org/10.1029/2007GL030168

Schepanski, K., Tegen, I., Todd, M.C., Heinold, B., Bönisch, G., Laurent, B., et al. (2009). Meteorological processes forcing Saharan dust emission inferred from MSG-SEVIRI observations of sub-daily dust source activation. Journal of Geophysical Research, 114, D10201. https://doi.org/10.1029/2008JD010325

Schepanski, K., Heinold, B., & Tegen, I. (2017). Harmattan, Saharan heat low, and West African monsoon circulation: modulations on the Saharan dust outflow towards the North Atlantic, Atmospheric Chemistry and Physics 17, 10223-10243. https://doi.org/10.5194/acp-17-10223-2017

Sorribas, M., Adame, J.A., Andrews, E., Yela, M. (2017). An anomalous African dust event and its impact on aerosol radiative forcing on the Southwest Atlantic coast of Europe in February 2016. Science of the Total Environment, 583, 269–279. https://doi.org/10.1016/j.scitotenv.2017.01.064

Strong, C., & Magnusdottir, G. (2008). Tropospheric Rossby wave breaking and the NAO/NAM. Journal of the Atmospheric Sciences, 65, 2861–2876. https://doi.org/10.1175/2008JAS2632.1

Thorncroft, C.D., Flocas, H.A. (1997). A Case Study of Saharan Cyclogenesis. Monthly Weather Review, 125, 1147-1165.

Thorncroft, C.D., Hoskins, B.J. (1990). Frontal cyclogenesis. Journal of the Atmospheric Sciences, 47, 2317-2336.

Thorncroft, C.D., Hoskins, B.J., McIntyre, M. E. (1993). Two paradigms of baroclinic wave life-cycle behaviour. Quarterly Journal of the Royal Meteorological Society, 119, 17–55.

Titos, G., Ealo, M., Pandolfi, M., Pérez, N., Sola, Y., Sicard, M., et al. (2017). Spatiotemporal evolution of a severe winter dust event in the western Mediterranean: Aerosol optical and physical properties. Journal of Geophysical Research: Atmospheres, 122, 4052–4069. https://doi.org/10.1002/2016JD026252

Tripoli, G.J., & Cotton, W.R. (1989). A numerical study of an observed orogenic mesoscale convective system. Part II: Analysis of governing dynamics. Monthly Weather Review, 117, 305–328. https://doi.org/10.1175/1520-0493(1989)117<0305:NSOAOO>2.0.CO;2

Varga, G., Újvári, G., & Kovácks, J. (2014). Spatiotemporal patterns of Saharan dust outbreaks in the Mediterranean Basin. Aeolian Research, 15, 151–160. https://doi.org/10.1016/j.aeolia.2014.06.005

Wernli H. & Sprenger M. (2007). Identification and ERA-15 climatology of potential vorticity streamers and cutoffs near the extratropical tropopause. Journal of the Atmospheric Sciences 64: 1569–1586.

Wiegand L., Knippertz P. (2014). Equatorward breaking Rossby waves over the North Atlantic and Mediterranean region in the ECMWF operational Ensemble Prediction System. Quarter Journal of the Royal Meteorological Society, 140, 58–71. DOI:10.1002/qj.2112

Zhang, F., & Koch, S.E. (2000). Numerical simulations of a gravity wave event over CCOPE. Part II: Waves generated by an orographic density current. Monthly Weather Review, 128, 2777–2796. https://doi.org/10.1175/1520-0493(2000)128<2777:NSOAGW>2.0.CO;2

Figure Captions

Figure 1. Sequence of MSG-SEVIRI dust RGB images to illustrate the development of convective clouds and haboob formation in the September 2007 case. White lines indicate relevant dust fronts. Terrain contours at 500 m intervals.

Figure 2. As in Figure 1 but for the October 2008 case.

Figure 3. As in Figure 1 but for the February 2016 case. The white oval indicates where and when dust mobilization starts to become visible.

Figure 4. Potential vorticity (shaded), wind vectors and Montgomery stream function (red contours) at the 330K surface for the ten days preceding the arrival of dust to the IP on the September 2007 case. The green circle in the plot of September 4 indicates the same position as in the vertical cross section of Figure 10a.

Figure 5. As in Figure 4 but for the October 2008 case. The green circle in the plot of October 8 indicates the same position as in the vertical cross section of Figure 10b.

Figure 6. As in Figure 4 but for the February 2016 case. The green circle in the plot of February 20 indicates the same position as in the vertical cross section of Figure 10c.

Figure 7. Mean sea level pressure (shaded), 925 hPa wind vectors and potential temperature (read contours) at the same time instants in September 2007 as in Figure 4.

Figure 8. As in Figure 7 but for October 2008 at the same time instants as in Figure 5.

Figure 9. As in Figure 7 but for February 2016 at the same time instants as in Figure 6.

Figure 10. Vertical-meridional cross sections of potential temperature (line contours), and v and omega wind components (arrows) just before development of convection, for the three case studies: (a) September 2007, (b) October 2008, and (c) February 2016.

Figure 11. Convective available potential energy (red contours) and relative humidity (shaded) at 925 hPa at the same time instants in September 2007 as in Figure 4.

Figure 12. As in Figure 11 but for October 2008 at the same time instants as in Figure 5.

Figure 13. 2m air temperature and 10m wind at 12 UTC for the February 2016 case

Figure 14. Skew T-log p diagrams of 00UTC soundings from Dar el Beida (DAAG, 60390) in Algeria.

Figure 15. Schematic depiction of the interactions between the two polar stream Rossby wave breaks that prepare the environment for moist convection and/or mountain wave formation over North Africa, responsible for dust ablation. The western location of RWB #2 favors dust transport poleward to southwestern Europe.

Figure 16. Schematic illustration of upper-level jet circulations (blue); near-surface flows (black) that undercut the stable Saharan air layer; jet streak secondary circulations (dashed black lines) and areas over the Atlas and Hoggar Mountains of intense differential heating leading to mountain plain solenoidal circulations (in red), both amplifying low-level convergence and divergence aloft.

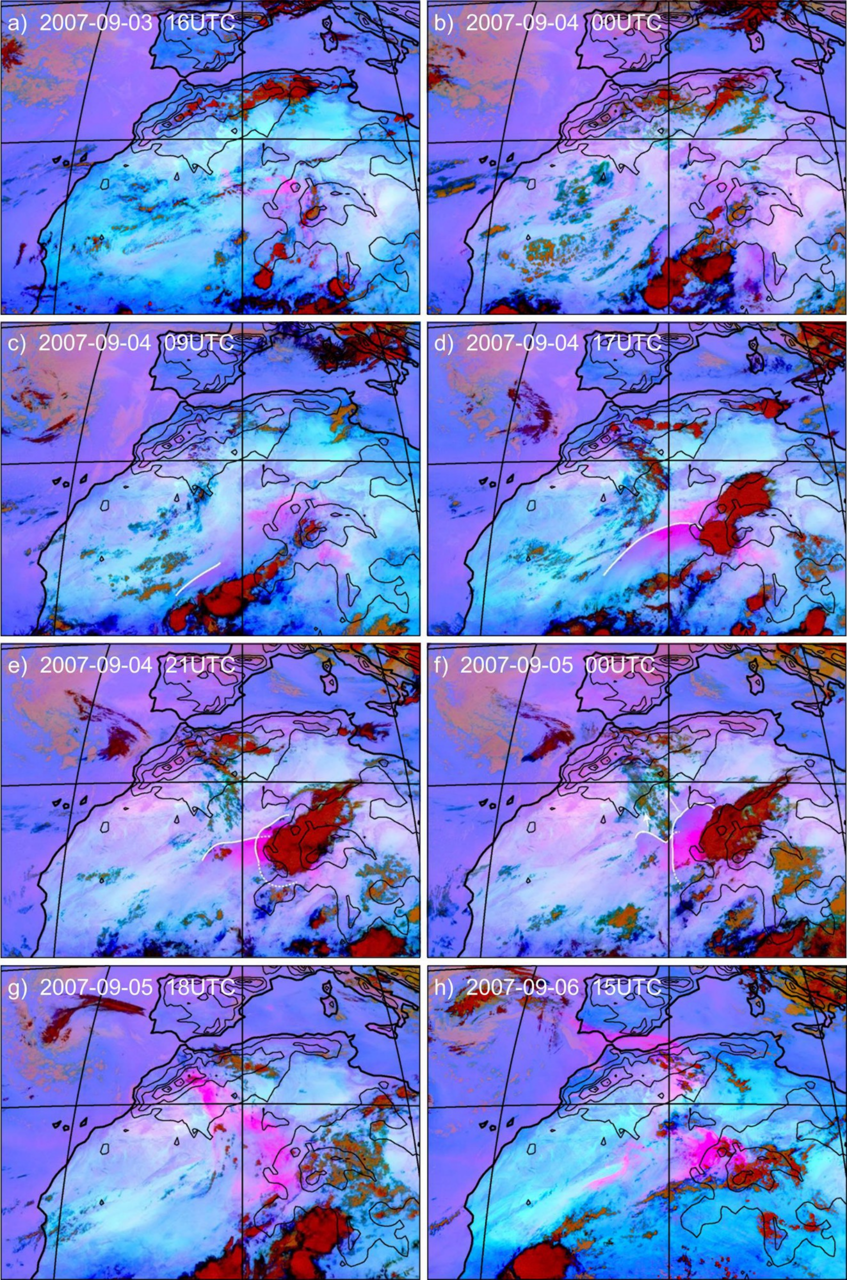
a) 2007-09-03 16UTC
b) 2007-09-04 00UTC
c) 2007-09-04 09UTC
d) 2007-09-04 17UTC
e) 2007-09-04 21UTC
f) 2007-09-05 00UTC
g) 2007-09-05 18UTC
h) 2007-09-06 15UTC

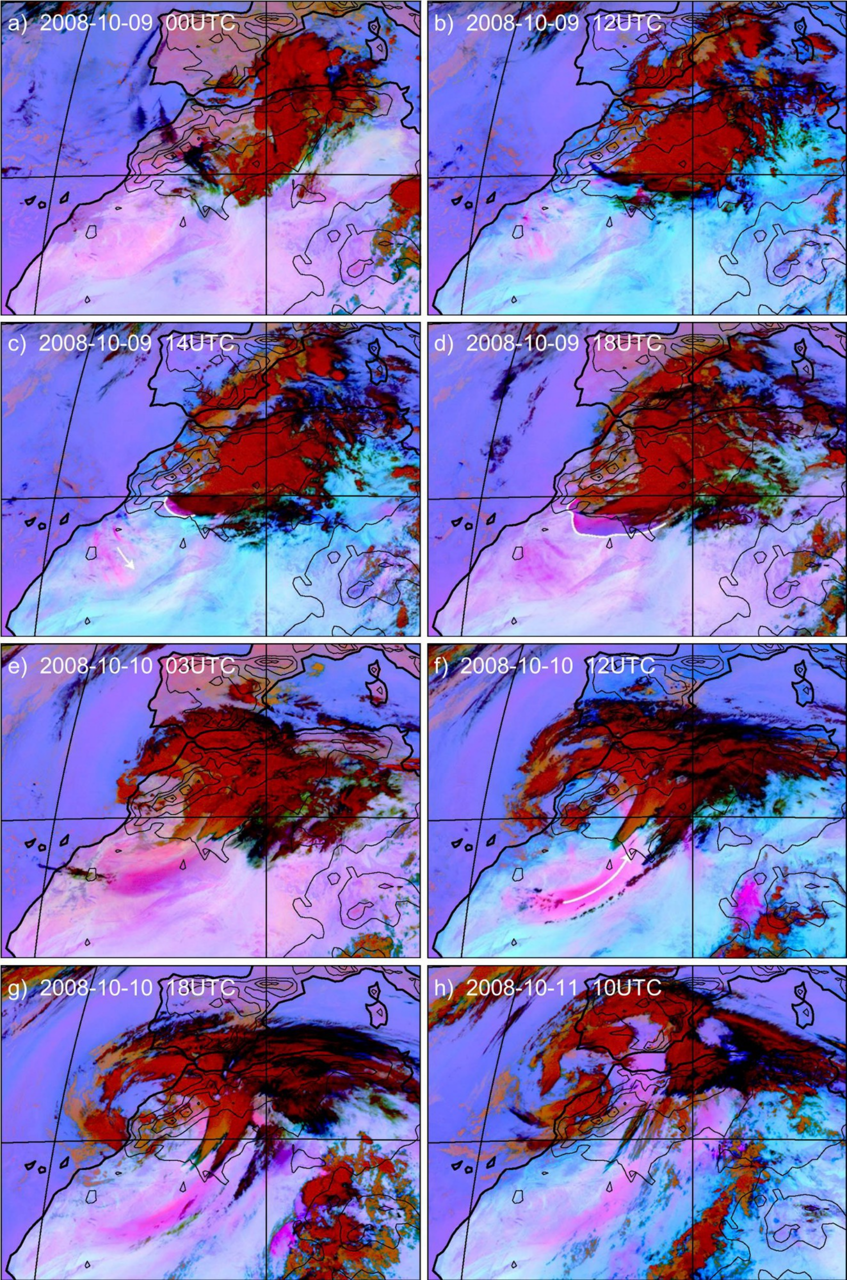
a) 2008-10-09 00UTC
b) 2008-10-09 12UTC
c) 2008-10-09 14UTC
d) 2008-10-09 18UTC
e) 2008-10-10 03UTC
f) 2008-10-10 12UTC
g) 2008-10-10 18UTC
h) 2008-10-11 10UTC

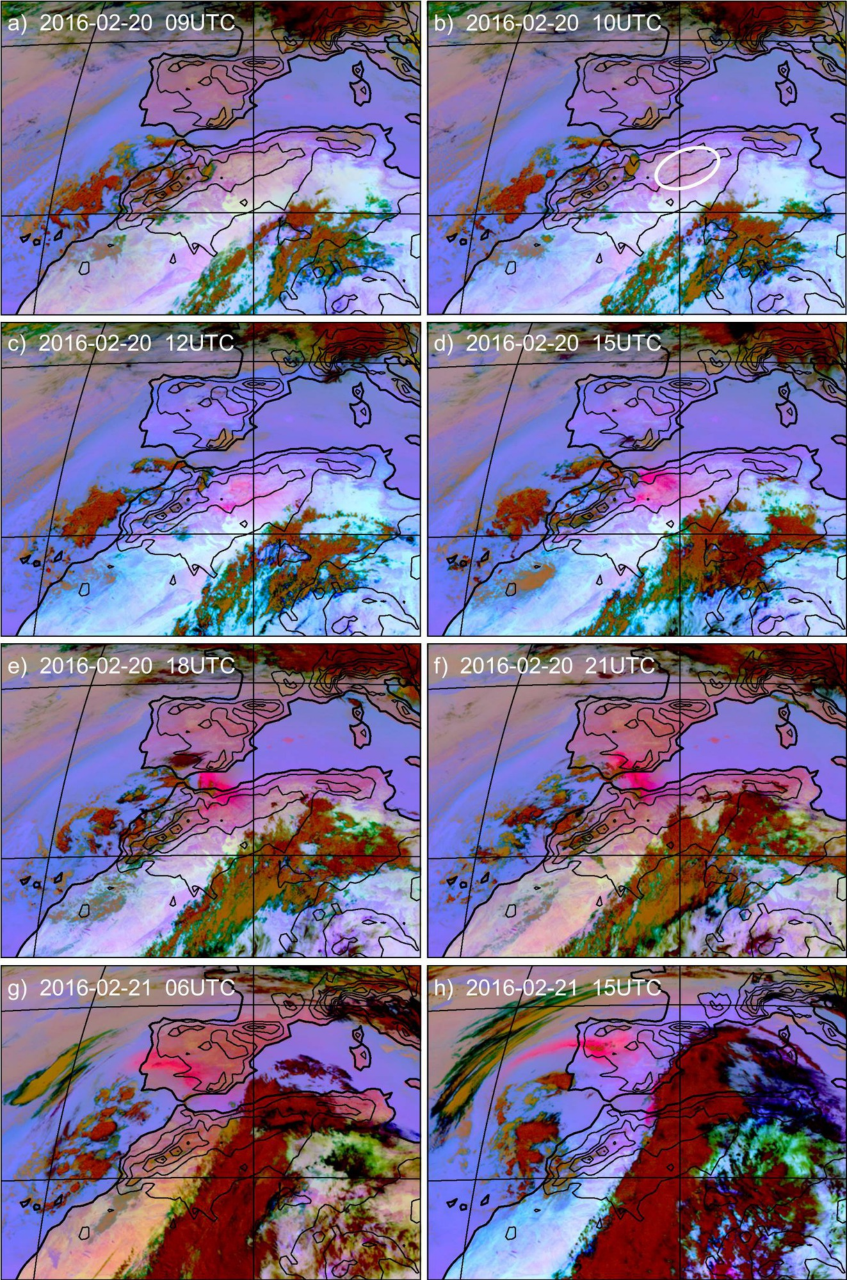
a) 2016-02-20 09UTC
b) 2016-02-20 10UTC
c) 2016-02-20 12UTC
d) 2016-02-20 15UTC
e) 2016-02-20 18UTC
f) 2016-02-20 21UTC
g) 2016-02-21 06UTC
h) 2016-02-21 15UTC

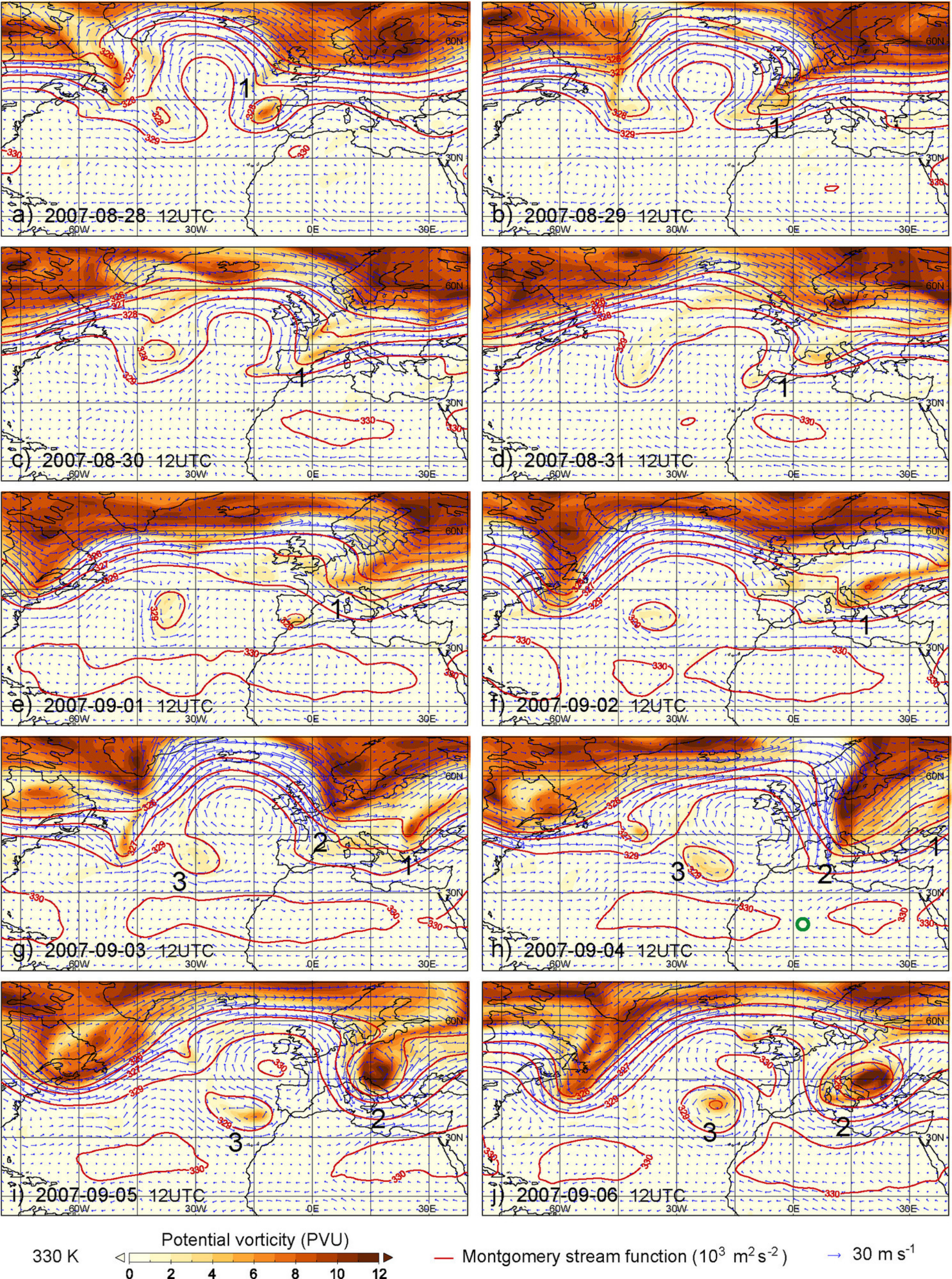

a) 2007-08-28 12UTC
b) 2007-08-29 12UTC
c) 2007-08-30 12UTC
d) 2007-08-31 12UTC
e) 2007-09-01 12UTC
f) 2007-09-02 12UTC
g) 2007-09-03 12UTC
h) 2007-09-04 12UTC
i) 2007-09-05 12UTC
j) 2007-09-06 12UTC
60W
30W
0E
30E
60N
30N
330 K
Potential vorticity (PVU)
0 2 4 6 8 10 12
Montgomery stream function (10^3 $m^2 s^{-2}$)
30 m s^{-1}

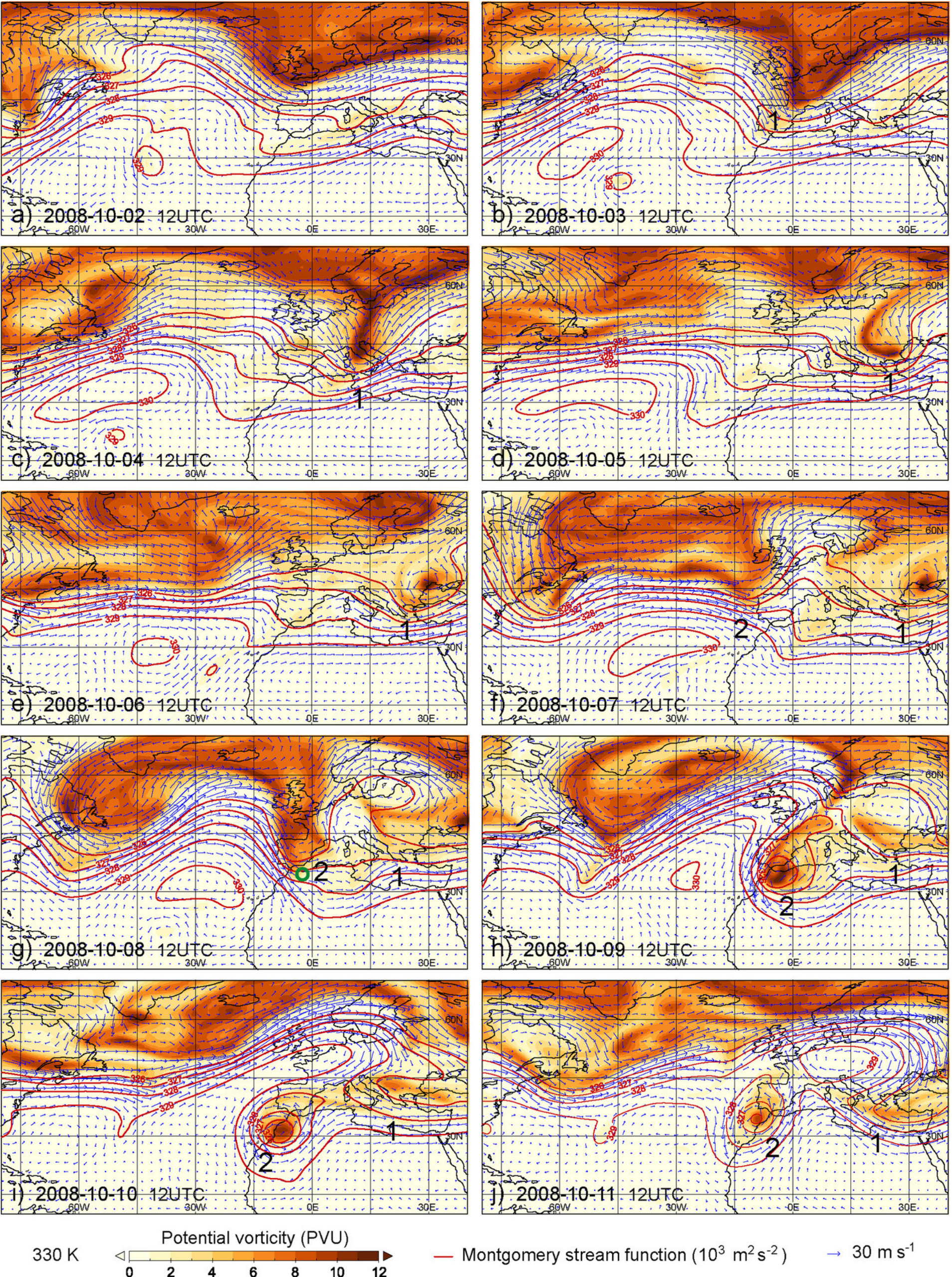

a) 2008-10-02 12UTC
b) 2008-10-03 12UTC
c) 2008-10-04 12UTC
d) 2008-10-05 12UTC
e) 2008-10-06 12UTC
f) 2008-10-07 12UTC
g) 2008-10-08 12UTC
h) 2008-10-09 12UTC
i) 2008-10-10 12UTC
j) 2008-10-11 12UTC
60W
30W
0E
30E
30N
60N
1
2
330 K
Potential vorticity (PVU)
0 2 4 6 8 10 12
Montgomery stream function (10^3 $m^2 s^{-2}$)
30 m s^{-1}

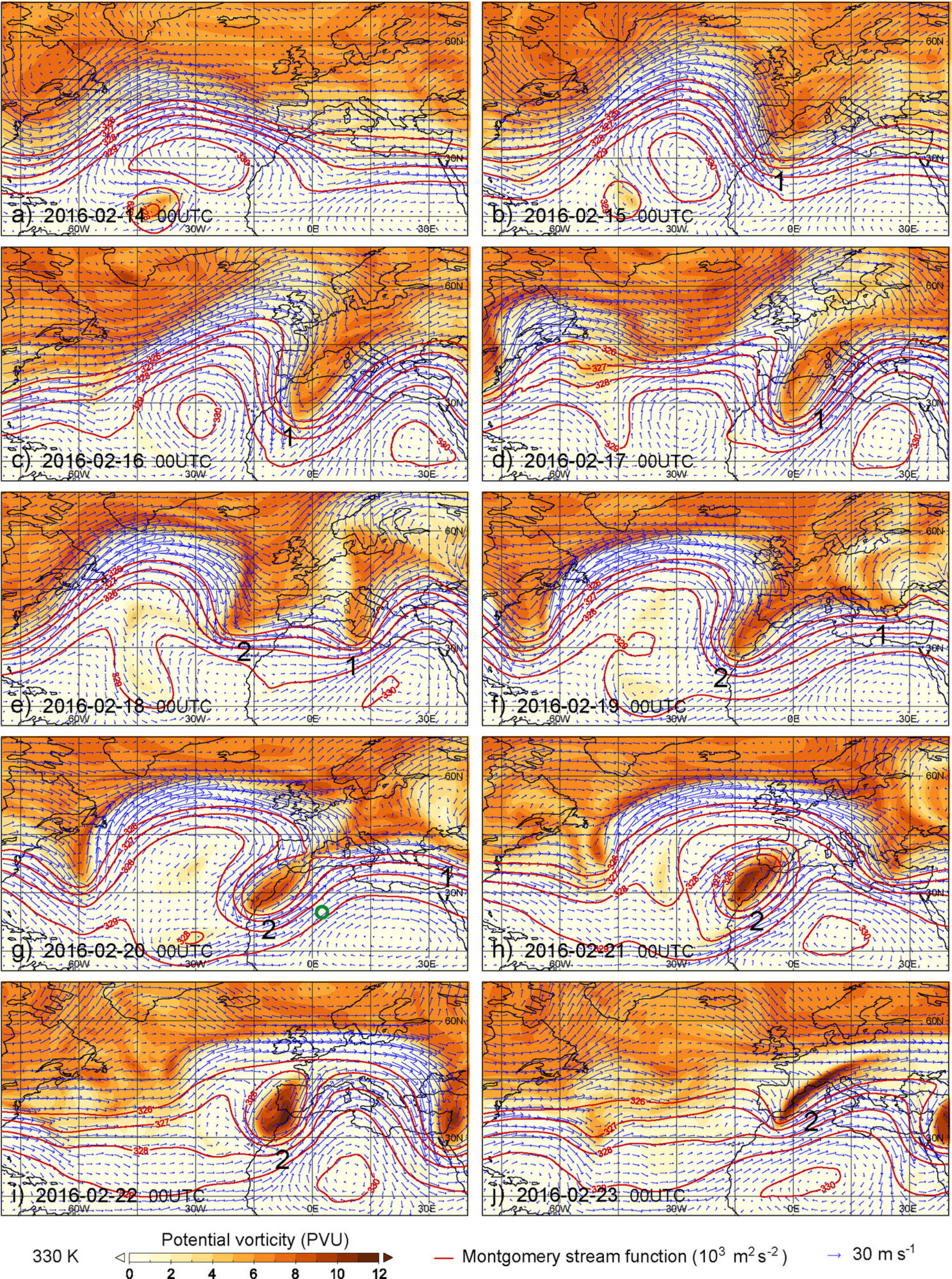
a) 2016-02-14 00UTC
b) 2016-02-15 00UTC
c) 2016-02-16 00UTC
d) 2016-02-17 00UTC
e) 2016-02-18 00UTC
f) 2016-02-19 00UTC
g) 2016-02-20 00UTC
h) 2016-02-21 00UTC
i) 2016-02-22 00UTC
j) 2016-02-23 00UTC
60W
30W
0E
30E
30N
60N
330 K
Potential vorticity (PVU)
0 2 4 6 8 10 12
Montgomery stream function (10^3 $m^2 s^{-2}$)
30 $m s^{-1}$

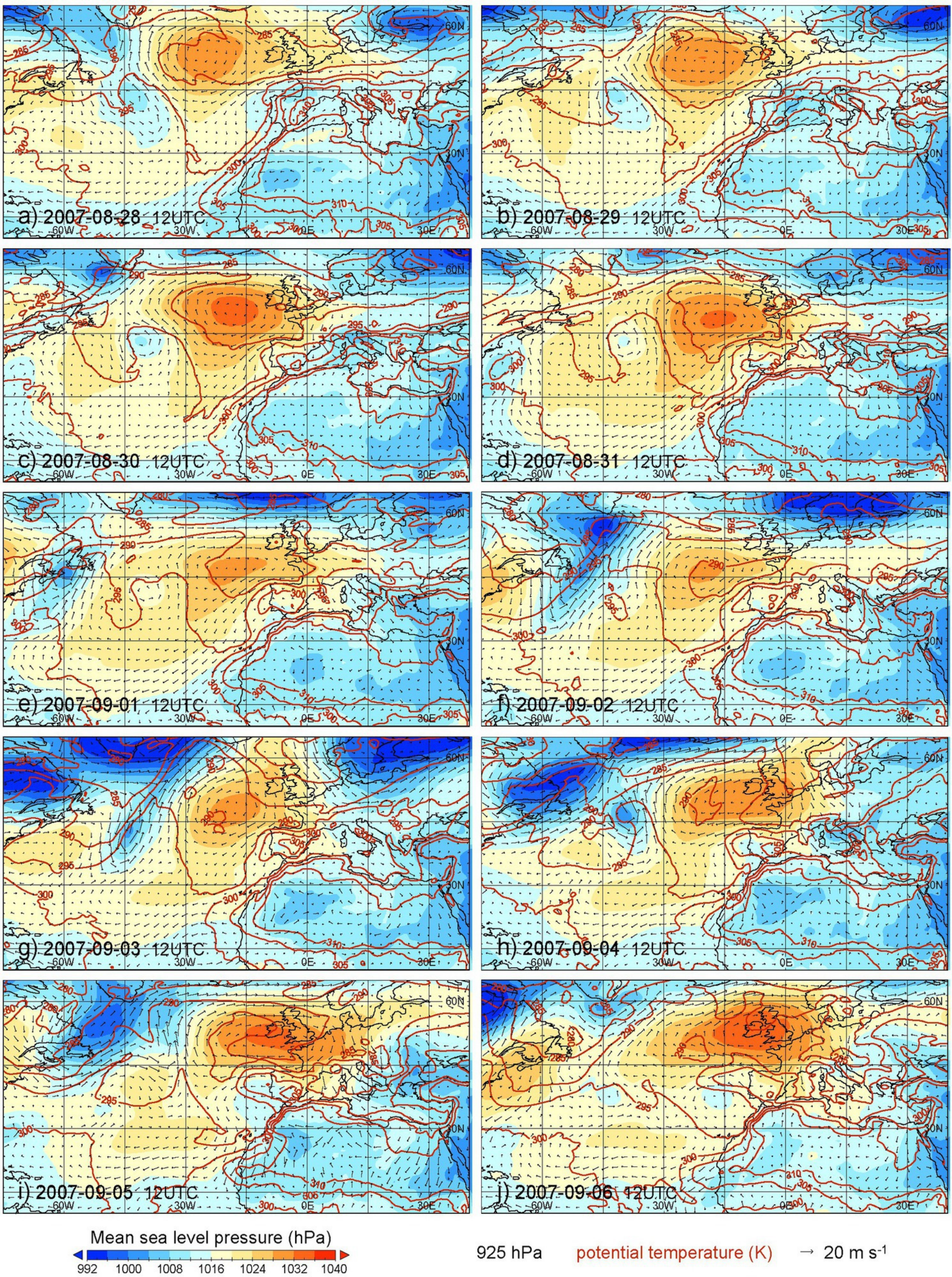
a) 2007-08-28 12UTC
b) 2007-08-29 12UTC
c) 2007-08-30 12UTC
d) 2007-08-31 12UTC
e) 2007-09-01 12UTC
f) 2007-09-02 12UTC
g) 2007-09-03 12UTC
h) 2007-09-04 12UTC
i) 2007-09-05 12UTC
j) 2007-09-06 12UTC
60W
30W
0E
30E
30N
60N
Mean sea level pressure (hPa)
992 1000 1008 1016 1024 1032 1040
925 hPa
potential temperature (K)
→ 20 m s-1

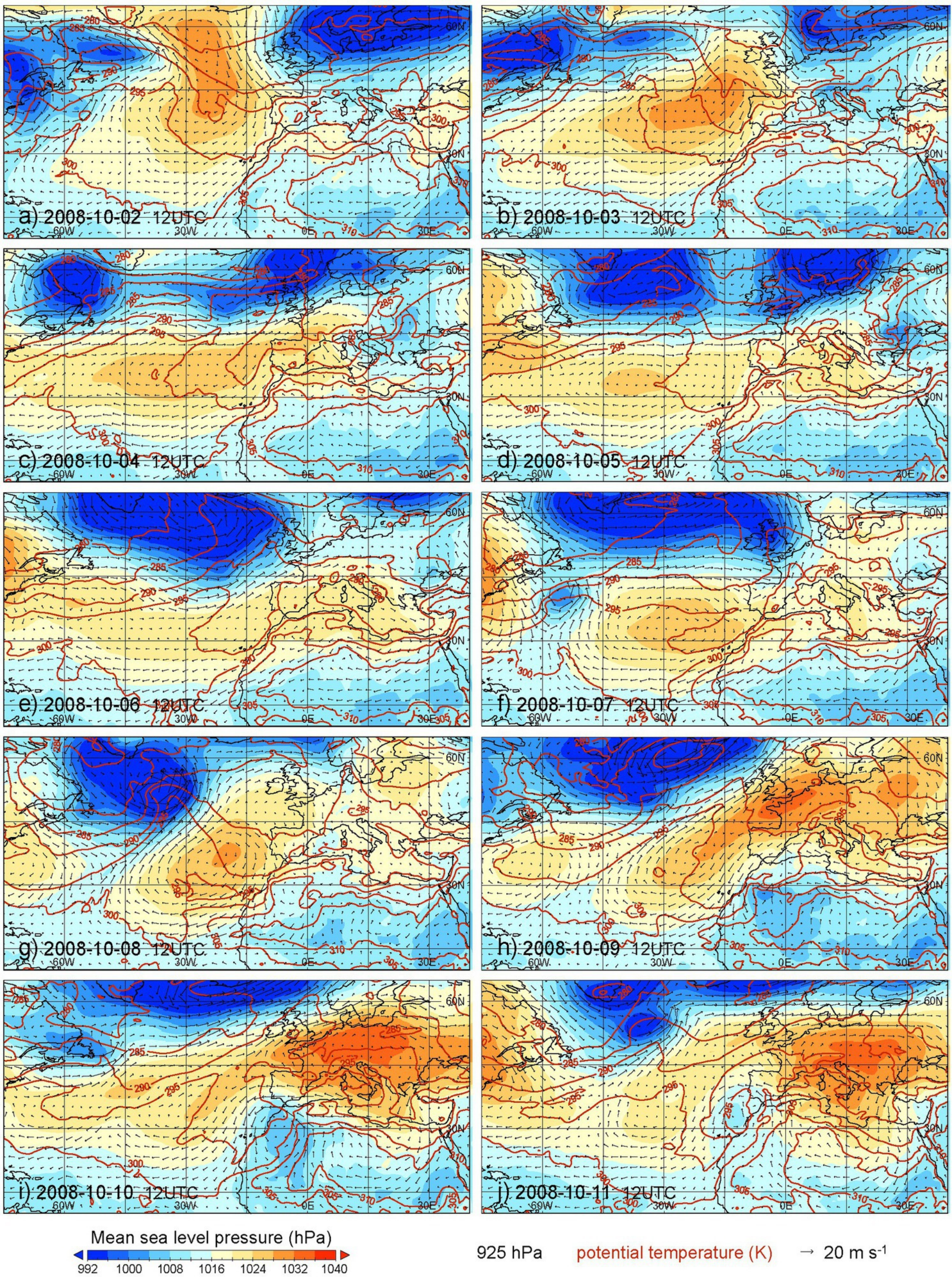
a) 2008-10-02 12UTC
b) 2008-10-03 12UTC
c) 2008-10-04 12UTC
d) 2008-10-05 12UTC
e) 2008-10-06 12UTC
f) 2008-10-07 12UTC
g) 2008-10-08 12UTC
h) 2008-10-09 12UTC
i) 2008-10-10 12UTC
j) 2008-10-11 12UTC
Mean sea level pressure (hPa)
992 1000 1008 1016 1024 1032 1040
925 hPa
potential temperature (K)
→ 20 m s-1

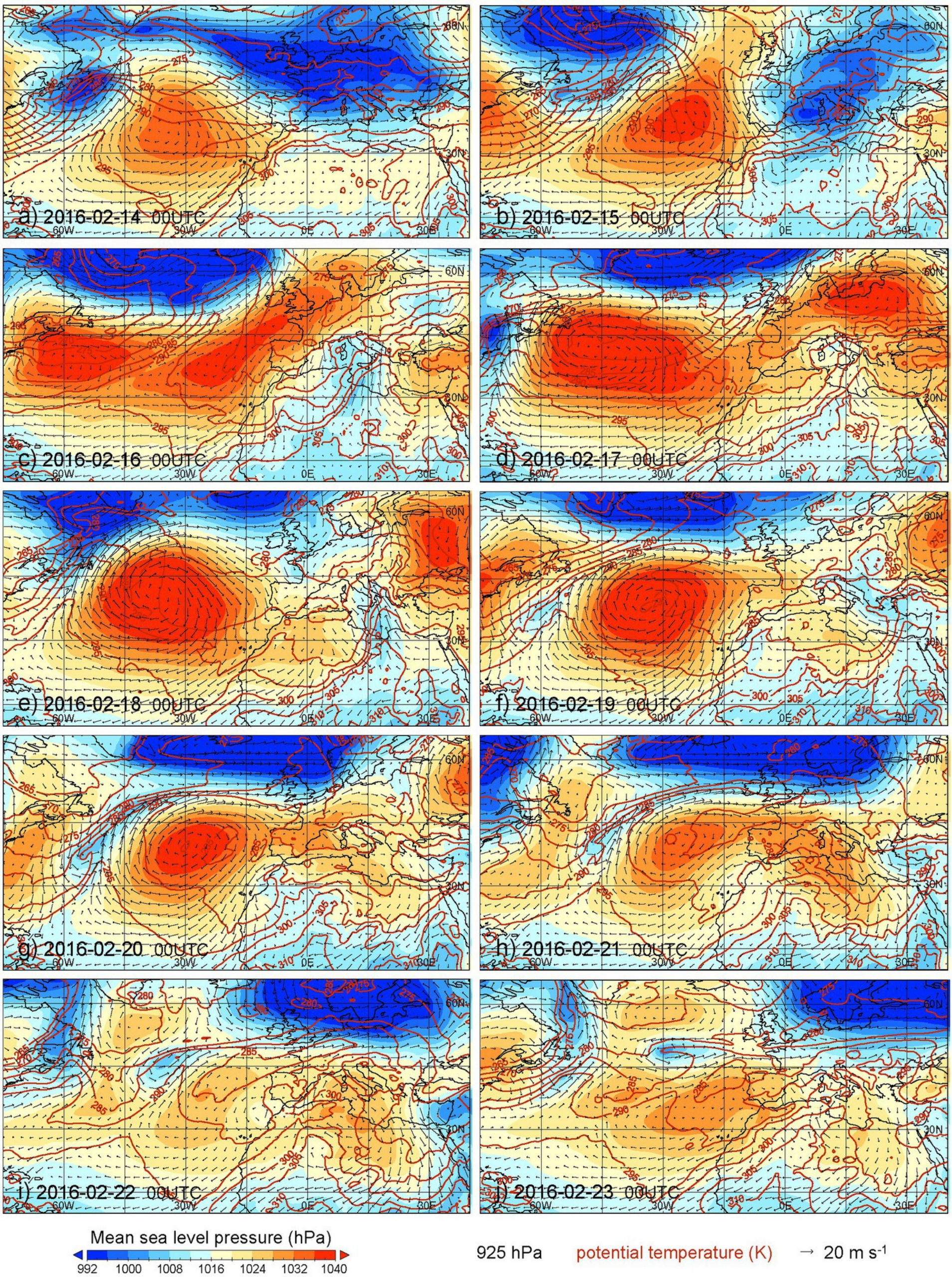
a) 2016-02-14 00UTC
b) 2016-02-15 00UTC
c) 2016-02-16 00UTC
d) 2016-02-17 00UTC
e) 2016-02-18 00UTC
f) 2016-02-19 00UTC
g) 2016-02-20 00UTC
h) 2016-02-21 00UTC
i) 2016-02-22 00UTC
j) 2016-02-23 00UTC
Mean sea level pressure (hPa)
992 1000 1008 1016 1024 1032 1040
925 hPa
potential temperature (K)
→ 20 m s-1

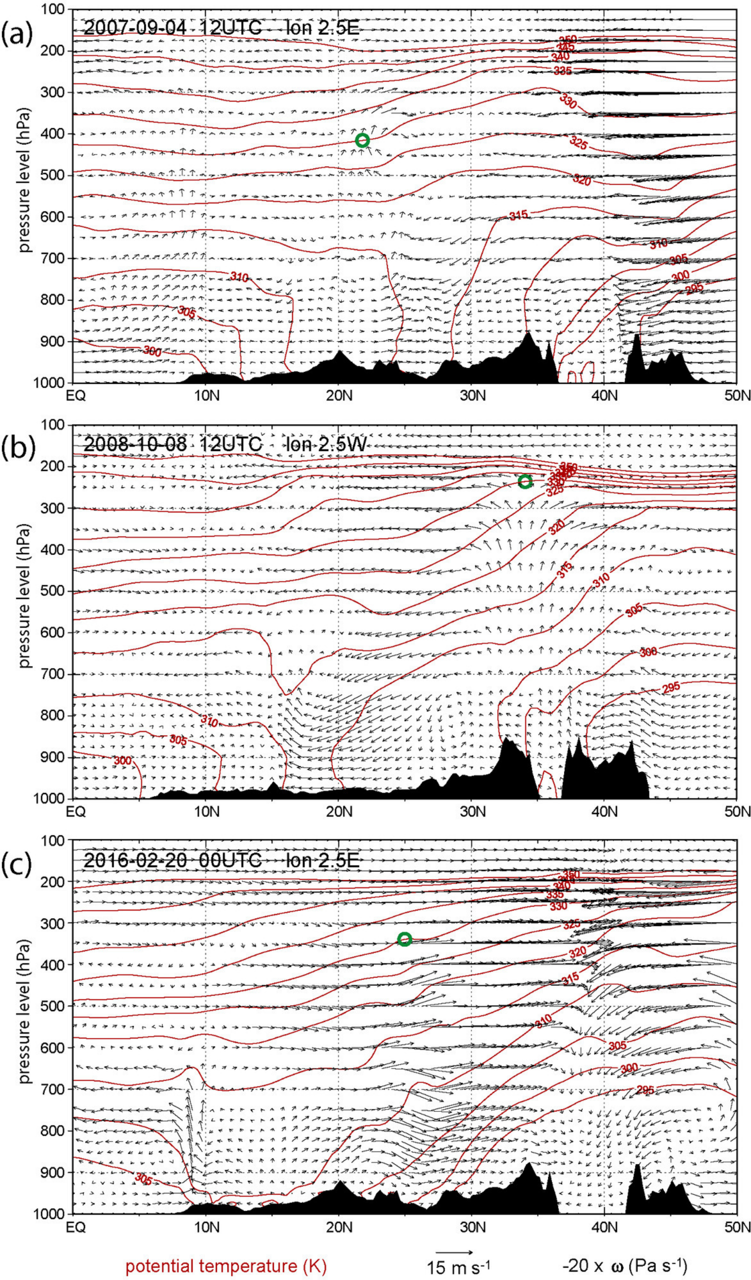
(a)
2007-09-04 12UTC lon 2.5E
(b)
2008-10-08 12UTC lon 2.5W
(c)
2016-02-20 00UTC lon 2.5E
pressure level (hPa)
EQ
10N
20N
30N
40N
50N
potential temperature (K)
15 m s-1
-20 x ω (Pa s-1)

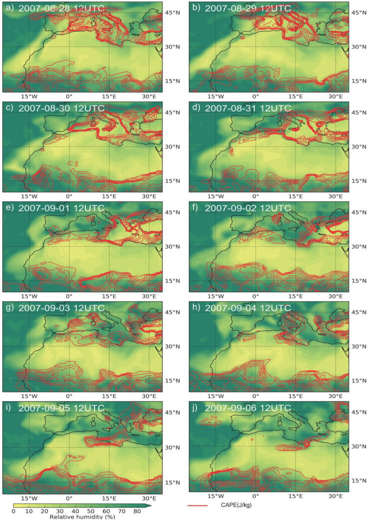
a) 2007-08-28 12UTC
b) 2007-08-29 12UTC
c) 2007-08-30 12UTC
d) 2007-08-31 12UTC
e) 2007-09-01 12UTC
f) 2007-09-02 12UTC
g) 2007-09-03 12UTC
h) 2007-09-04 12UTC
i) 2007-09-05 12UTC
j) 2007-09-06 12UTC
15°W
0°
15°E
30°E
45°N
30°N
15°N
0 10 20 30 40 50 60 70 80
Relative humidity (%)
CAPE(J/kg)

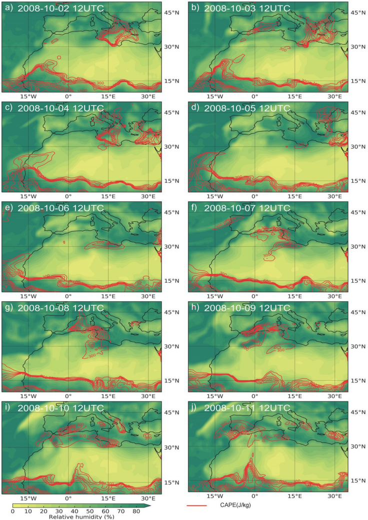

a) 2008-10-02 12UTC
b) 2008-10-03 12UTC
c) 2008-10-04 12UTC
d) 2008-10-05 12UTC
e) 2008-10-06 12UTC
f) 2008-10-07 12UTC
g) 2008-10-08 12UTC
h) 2008-10-09 12UTC
i) 2008-10-10 12UTC
j) 2008-10-11 12UTC
45°N
30°N
15°N
15°W
0°
15°E
30°E
0 10 20 30 40 50 60 70 80
Relative humidity (%)
CAPE(J/kg)

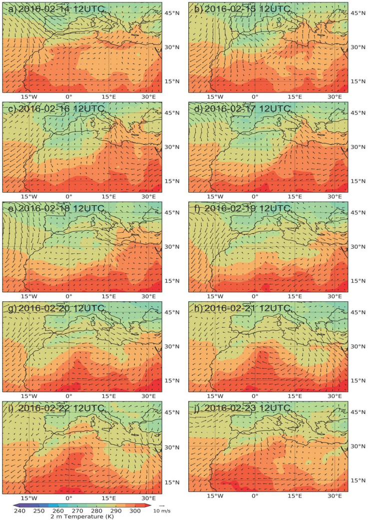
a) 2016-02-14 12UTC
b) 2016-02-15 12UTC
c) 2016-02-16 12UTC
d) 2016-02-17 12UTC
e) 2016-02-18 12UTC
f) 2016-02-19 12UTC
g) 2016-02-20 12UTC
h) 2016-02-21 12UTC
i) 2016-02-22 12UTC
j) 2016-02-23 12UTC
45°N
30°N
15°N
15°W
0°
15°E
30°E
240
250
260
270
280
290
300
2 m Temperature (K)
10 m/s

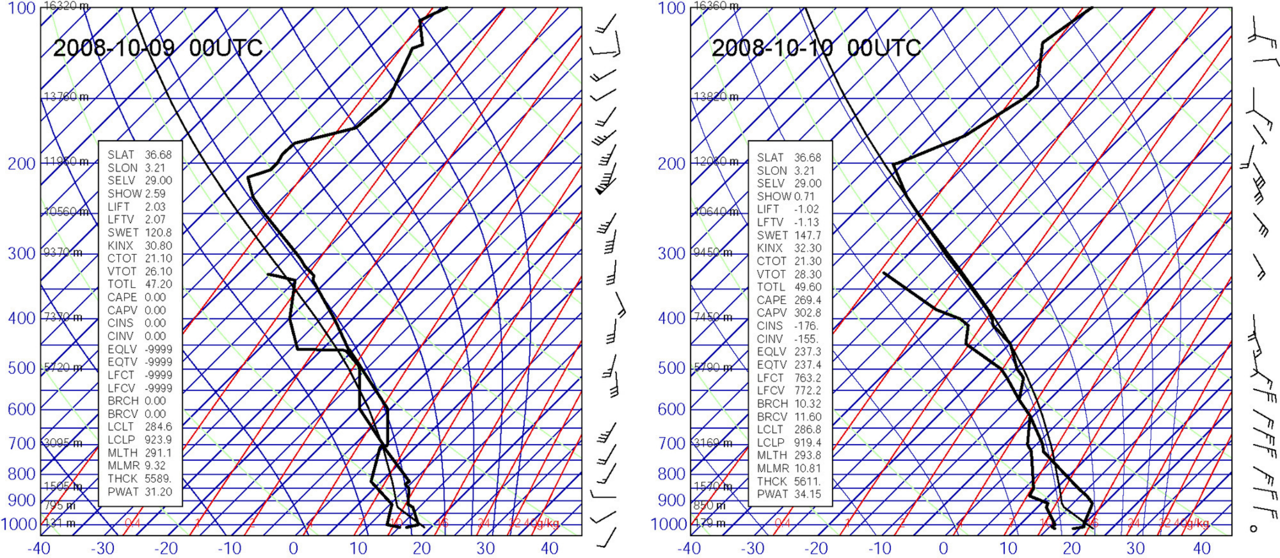

2008-10-09 00UTC
SLAT 36.68
SLON 3.21
SELV 29.00
SHOW 2.59
LIFT 2.03
LFTV 2.07
SWET 120.8
KINX 30.80
CTOT 21.10
VTOT 26.10
TOTL 47.20
CAPE 0.00
CAPV 0.00
CINS 0.00
CINV 0.00
EQLV -9999
EQTV -9999
LFCT -9999
LFCV -9999
BRCH 0.00
BRCV 0.00
LCLT 284.6
LCLP 923.9
MLTH 291.1
MLMR 9.32
THCK 5589.
PWAT 31.20
2008-10-10 00UTC
SLAT 36.68
SLON 3.21
SELV 29.00
SHOW 0.71
LIFT -1.02
LFTV -1.13
SWET 147.7
KINX 32.30
CTOT 21.30
VTOT 28.30
TOTL 49.60
CAPE 269.4
CAPV 302.8
CINS -176.
CINV -155.
EQLV 237.3
EQTV 237.4
LFCT 763.2
LFCV 772.2
BRCH 10.32
BRCV 11.60
LCLT 286.8
LCLP 919.4
MLTH 293.8
MLMR 10.81
THCK 5611.
PWAT 34.15

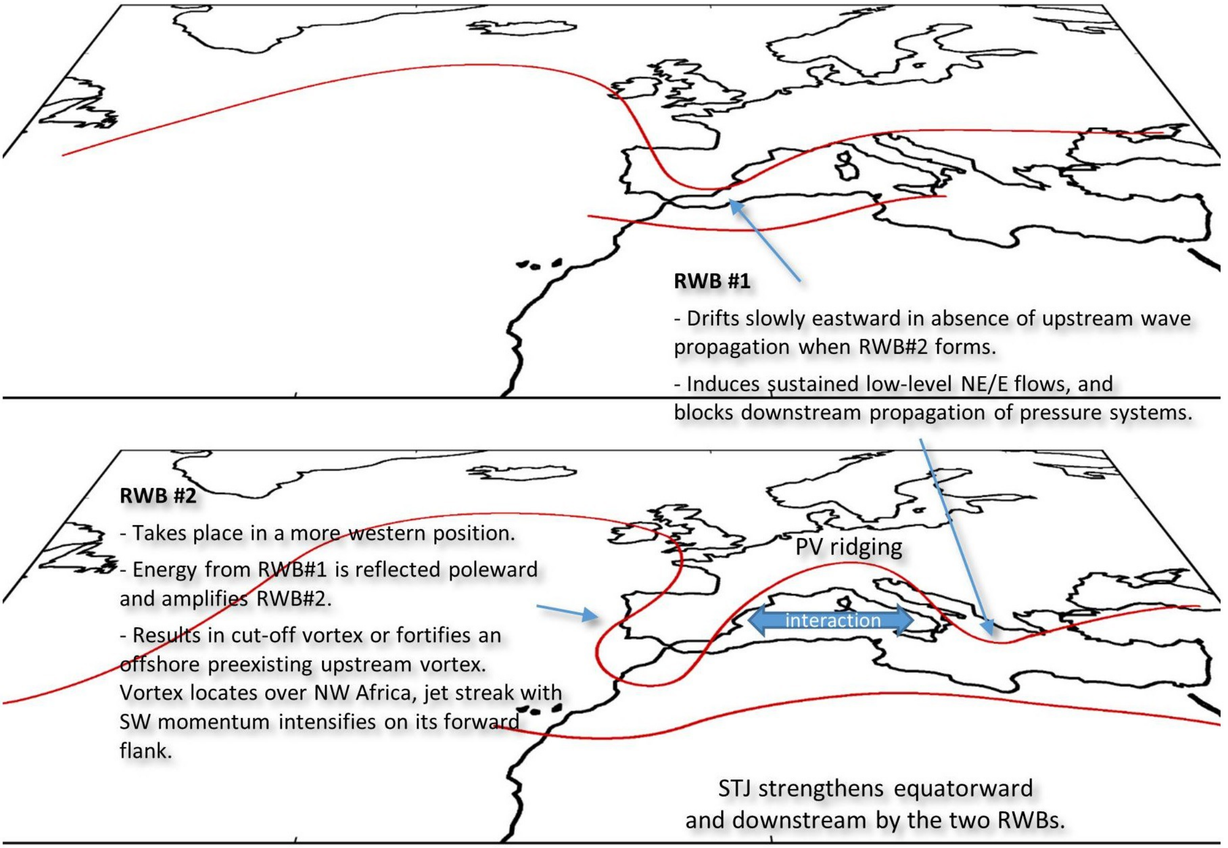

RWB #1
- Drifts slowly eastward in absence of upstream wave propagation when RWB#2 forms.
- Induces sustained low-level NE/E flows, and blocks downstream propagation of pressure systems.
RWB #2
- Takes place in a more western position.
- Energy from RWB#1 is reflected poleward and amplifies RWB#2.
- Results in cut-off vortex or fortifies an offshore preexisting upstream vortex. Vortex locates over NW Africa, jet streak with SW momentum intensifies on its forward flank.
PV ridging
interaction
STJ strengthens equatorward and downstream by the two RWBs.

Sep2007

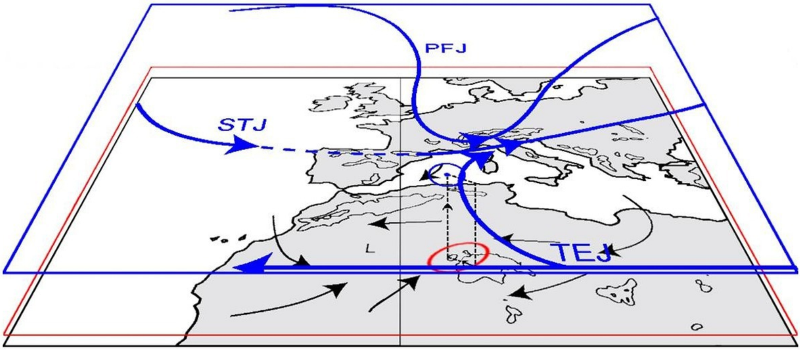

Oct2008

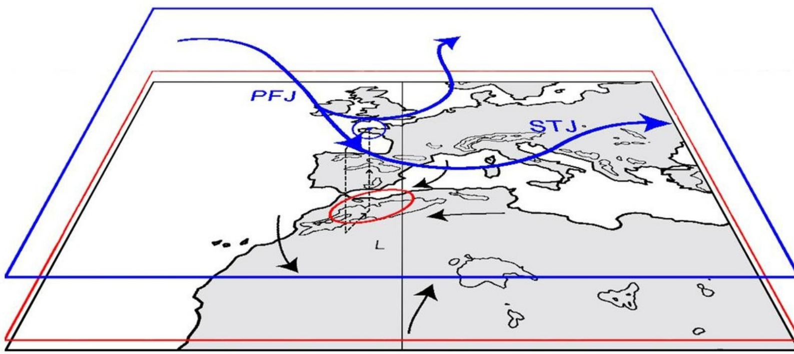

Feb2016